

A Comprehensive Study on Hot Deformation Behavior of the Metastable β Titanium Alloy Prepared by Blended Elemental Powder Metallurgy Approach



KRYSTIAN ZYGUŁA, OLEKSANDR LYPCHANSKYI, ANETA ŁUKASZEK-SOŁEK, GRZEGORZ KORPAŁA, RAFAŁ STANIK, MICHAŁ KUBIŚ, BARTŁOMIEJ PRZYBYSZEWSKI, MAREK WOJTASZEK, MAIK GUDE, and ULRICH PRAHL

The hot deformation behavior of a Ti–5Al–5Mo–5V–3Cr alloy obtained by the Blended Elemental Powder Metallurgy approach was studied. Hot compression tests were performed to determine the stress–strain relationships at temperatures ranging from 800 °C to 1000 °C and strain rates between 0.1 and 20 s⁻¹. Based on the collected data, a constitutive model was developed using an Arrhenius-type equation, and a deformation activation energy map was generated. Processing maps were created using the Dynamic Material Model theory, and a processing window indicating the optimal hot deformation parameters was determined at temperatures between 900 °C and 1000 °C and strain rates of 0.1–2.0 s⁻¹. Microstructure observations confirmed the results of the DMM analysis, with a homogeneous and recrystallized microstructure found under the processing window parameters. The hot-rolling process was designed using FEM modeling and was successfully verified by laboratory tests. The hot-rolling parameters selected based on previous analysis resulted in a fully compacted material with controlled microstructure. The relationship between the deformation parameters, microstructure, hardness, and tensile properties of the Ti–5Al–5Mo–5V–3Cr alloy after hot rolling was analyzed. Hot rolling using the developed thermomechanical parameters resulted in a significant increase in tensile strength from 757 to 1009 MPa. In general, this study provides a comprehensive characterization of the hot deformation behavior of the Ti–5Al–5Mo–5V–3Cr alloy and valuable insights for optimizing its hot-processing parameters.

<https://doi.org/10.1007/s11661-024-07297-9>

© The Minerals, Metals & Materials Society and ASM International 2024

I. INTRODUCTION

METASTABLE B titanium alloys have gained significant attention in the aviation industry due to their advantageous combination of low density, high strength, and good fatigue properties. In addition, these alloys exhibit good formability, enabling the production of structural components through hot deformation processes involving high strain values.^[1] Currently, the prevailing method for manufacturing titanium alloy products involves vacuum casting, followed by hot deformation and machining.^[2] Although vacuum casting allows for the production of high-quality titanium alloys, it is often considered costly due to the complexity of individual processes and material-consuming machining.^[3] A promising alternative to conventional processes is the use of powder metallurgy, which streamlines the manufacturing chain and enables the production of alloys with desired chemical compositions and near-net shape products, as demonstrated by Calvert *et al.*^[4]

KRYSTIAN ZYGUŁA, ANETA ŁUKASZEK-SOŁEK, and MAREK WOJTASZEK are with the Faculty of Metals Engineering and Industrial Computer Science, AGH University of Krakow, Al. A. Mickiewicza 30, 30-059 Kraków, Poland. Contact e-mail: kzygula@agh.edu.pl OLEKSANDR LYPCHANSKYI is with the Faculty of Metals Engineering and Industrial Computer Science, AGH University of Krakow and also with the Institut für Metallformung, TU Bergakademie Freiberg, Bernhard-von-Cotta-Straße 4, 09599 Freiberg, Germany. GRZEGORZ KORPAŁA and ULRICH PRAHL are with the Institut für Metallformung, TU Bergakademie Freiberg. RAFAŁ STANIK and MAIK GUDE are with the Institute of Lightweight Engineering and Polymer Technology (ILK), Technische Universität Dresden, Holbeinstraße 3, 01307 Dresden, Germany. MICHAŁ KUBIŚ is with the Faculty of Power and Aeronautical Engineering, Institute of Heat Engineering, Warsaw University of Technology, Nowowiejska St. 21/25, 00-665 Warsaw, Poland. BARTŁOMIEJ PRZYBYSZEWSKI is with the Faculty of Materials Science and Engineering, Warsaw University of Technology, Woloska 141, 02-507 Warsaw, Poland.

Manuscript submitted July 7, 2023; accepted December 26, 2023.

Article published online January 30, 2024

Typically, master powders or a mixture of pure hydride-dehydride (HDH) titanium powder with master powders as alloying elements serves as base materials. This approach has been previously employed in the fabrication of titanium alloys numerous times.^[5,6] A more cost-effective approach involves the use of the Blended Elemental Powder Metallurgy (BEPM) method, as demonstrated by Ahmed *et al.*^[7] However, it is important to note that materials produced using this method carry a risk of compositional inhomogeneity and increased porosity. Therefore, semi-finished products derived from elemental powders are often subjected to additional hot deformation. However, the deformation of titanium alloys necessitates the careful selection of process parameters and a comprehensive understanding of the fundamental phenomena accompanying hot deformation, which directly impact changes in the microstructure and, consequently, the strength properties of the resulting products.^[8]

During hot deformation, various phenomena occur in the material, which are influenced by the primary deformation parameters: temperature, strain rate, and strain value. These phenomena lead to the evolution of the microstructure and can involve mechanisms of both strain hardening and softening. Strain hardening is dependent on the deformation parameters and results in an increase in flow stress during the initial stages of deformation. The extent of this effect is more pronounced at lower temperatures or higher strain rates. Conversely, under certain conditions, softening phenomena occur after surpassing a critical strain value. These softening mechanisms can include dynamic recovery (DRV) and dynamic recrystallization (DRX), which serve to counteract the effects of deformation and remodel the microstructure. The driving force behind these microstructure remodeling mechanisms is the strain energy generated during hot forming. The process of DRV in the deformation of titanium alloys has been described by Zhao *et al.*^[9] DRV typically occurs at low strain rates and involves dislocation movement through sliding, climbing, or cross-sliding to reduce internal stresses. Further displacement of dislocations leads to the formation of sub-grains or new low-angle grain boundaries (LAGBs). The microstructure resulting from DRV during hot deformation is characterized by slightly flattened grains elongated in the direction perpendicular to the applied force and serrated grain boundaries. DRV is more prevalent in materials with high stacking fault energy, where dislocation movement is facilitated. Titanium alloys fall into this category, making DRV a favorable process for the subsequent occurrence of DRX.^[10]

High strain levels during hot deformation promote the occurrence of DRX. Under such conditions, a complete remodeling of the microstructure takes place, leading to homogenization. The microstructural changes during DRX can be categorized into two in the initial stages of hot deformation, the β phase exists in the form of equiaxed grains. As deformation progresses, dislocations begin to appear, primarily concentrated at the grain boundaries. With increasing strain, an initial stage of DRV occurs, resulting in the formation of a

substructure characterized by high-angle grain boundaries (HAGBs). The driving force behind DRX is generally the energy stored in dislocations. If the strain energy accumulated at the boundaries of the original β phase grains reaches a critical level, nucleation of new grains is initiated. The HAGBs of the newly formed grains undergo migration, leading to grain growth, and continuous absorption of dislocations. Nucleation and growth of new grains continue during this stage, resulting in the development of a fine and homogeneous microstructure. If the deformation process continues, recrystallized grains may undergo further deformation and secondary recovery, leading to the appearance of elongated, serrated grain boundaries.

The behavior of materials during hot deformation can be predicted using phenomenological constitutive models or physically based constitutive models. In recent years, numerous studies have described the phenomena occurring during hot processing by developing constitutive models. For instance, a constitutive model for titanium alloy during deformation in the $\alpha + \beta$ range has been developed using an artificial neural network.^[11] However, constitutive models are more commonly used for frequently employed alloys. For example, Lypchanskyi *et al.*^[12] employed constitutive equations to describe the behavior of commercially available aerospace titanium alloys. Presently, constitutive analyses are also being conducted on β titanium alloys produced from powders.^[13] Nevertheless, it is worth noting that a comprehensive description of the behavior of materials entirely composed of elemental powders is lacking in the literature. The Arrhenius-type constitutive equation is the most commonly employed model, which accurately predicts the flow stress during the deformation of titanium alloys.^[14] Additionally, the prediction of microstructure evolution is often described using processing maps.

Trials of real hot deformation processes are known to be expensive and time consuming. Therefore, Finite Element Method (FEM) simulations are employed to support the design of hot-forming processes. In combination with processing maps analysis, FEM modeling allows for the assessment of the accuracy of forging parameters for various alloys. For instance, the authors of Reference 15 used FEM modeling and processing maps analysis to evaluate the correctness of forging parameters for a nickel-based superalloy. By employing numerical calculations, the impact of selected forming parameters on temperature distribution, stress distribution, and strain distribution within the material can be determined. Furthermore, the necessary forces required for the operation of the machine can be determined, and the formation of defects in the final product can be predicted.^[4] Thus, FEM simulations provide valuable insights for optimizing the hot-forming process and ensuring the quality of the resulting products.

In recent years, there has been significant research focused on the hot-rolling process of titanium alloys, with particular emphasis on the evolution of the microstructure. Alongside changes in material shape, significant changes occur in the microstructure during hot deformation. The size and morphology of α grains in

titanium alloys play a crucial role in determining their mechanical properties. Kang and Yang^[16] widely discussed the influence of different microstructure types on mechanical properties. The type of microstructure that emerges after hot deformation depends on the processing temperature. If the material is deformed above the β -transus temperature, the predominant microstructure after cooling will be a fine-equiaxed structure. On the other hand, if the deformation temperature is lower than the β -transus temperature, a structure consisting of fragmented α lamellae will form. It is important to note that the microstructure type can be precisely tailored by controlling deformation parameters such as temperature, strain rate, or cooling rate. Constitutive modeling, as described in the previous paragraph, can be a valuable approach to achieving the desired microstructure and corresponding mechanical properties.

The objective of this research was to comprehensively characterize the hot deformation and microstructure evolution of the metastable Ti-5553 alloy prepared using the powder metallurgy route. The powder mixture was hot compacted through a uniaxial hot-pressing process. Hot compression tests were conducted in the temperature range of 800 °C to 1000 °C and strain rates ranging from 0.1 to 20 s⁻¹. The deformation behavior was characterized by analyzing flow curves, deformation activation energy, and processing maps. In addition, a constitutive model was developed. The results were validated through microstructure observations following the hot compression tests. Furthermore, based on selected hot deformation parameters and supported FEM modeling, a hot-rolling process was designed. The process was verified through hot-rolling tests, and the microstructure and mechanical properties after hot deformation were analyzed.

II. EXPERIMENTAL PROCEDURE

The investigated material is the metastable β titanium alloy with a nominal chemical composition of Ti-5Al-5Mo-5V-3Cr (m. pct, Ti-5553). It was obtained using the Blended Elemental Powder Metallurgy (BEPM) method. The starting materials used in the mixing process were previously described in detail in References 17, 18. The mixture of elemental powders was uniaxially hot-pressed into a compact under an argon protective atmosphere for 45 minutes at a temperature of 1250 °C and a uniaxial pressure of 25 MPa. The relative density of the compact was measured using the Archimedes method and was found to be 98.2 ± 0.4 pct relative to the theoretical density of the solid material, which is 4.68 g/cm³. Non-destructive computed tomography (CT) testing of the compact was carried out using a v|tome|x L-450 CT scanner equipped with a 450 kV microfocuss lamp, with a minimum focal spot size of 1 μ m and a detector resolution of 2000 \times 2000 pixels. The results were analyzed using myVGL 3.0 software.

Cylindrical samples with dimensions of 10 mm in diameter and 18 mm in height were wire cut from the middle area of the Ti-5553 compact. Hot compression tests were conducted using the WUMSI

Servo-Hydraulic Hot Deformation Simulator in the temperature range of 800 °C to 1000 °C and strain rates of 0.1, 1, 10, and 20 s⁻¹. The maximum true strain value was 1.0. Each sample was placed in a heat-resistant steel compression beaker and heated in a furnace to a temperature of 1000 °C, holding it at this temperature for 10 minutes to homogenize the microstructure. The compression beaker ensured a homogeneous temperature distribution. High-temperature graphite lubricant was applied to both front surfaces of the samples to reduce friction forces. Subsequently, the sample was cooled to the deformation temperature and compressed. After deformation, the sample was removed from the compression beaker and cooled in water to preserve the deformation microstructure. Friction, strain rate, and adiabatic heating significantly influence the flow stress value. Therefore, to accurately determine the true stress value during a hot compression test, corrections must be made to account for these factors. In developing the flow curves, the necessary corrections were implemented using the Hensel–Spittel approach and the Siebel equation.^[19,20] Material data such as the friction coefficient, density, and thermal conductivity of the test material were used to accurately determine the true flow stress during correction.

The thermal properties of the investigated alloy, such as specific heat (C_p) and diffusivity (a), were determined using Differential Scanning Calorimetry (DSC) with the Netzsch 404 F1 Pegasus instrument, and Laser Flash Apparatus (LFA) with the Netzsch LFA 457 Micro-Flash, respectively. The thermal conductivity (λ) was determined using the indirect method, employing the formula $\lambda = aC_p\rho$, where ρ is measured density. To determine the friction coefficient at high temperatures, a ring compression test was performed using the Gleeble HDS-V 40 thermal physical simulator. A sample with dimensions of 12 mm in outer diameter, 6 mm in internal diameter, and 4 mm in height was conductively heated at a rate of 2.5 °C/s to a temperature of 900 °C. Subsequently, it was compressed at a strain rate of 1 s⁻¹ until reaching a true strain value of 0.3. The data obtained during the tests mentioned above were used to develop the FEM simulation of the hot-rolling process.

The hot-rolling process was performed using a three-high rolling mill. The Ti-5553 compact was cut into the shape of a bar with dimensions of 30 \times 30 \times 65 mm, then heated to the temperature of 1000 °C, and subjected to 7-pass hot-rolling procedure, with intermediate heating after 6 passes.

To determine the phase composition of the Ti-5553 compact and hot-rolled material, X-ray diffraction (XRD) analysis was conducted using Panalytical Empyrean DY 1061 with Cu K α radiation ($\lambda = 1.54$ nm). Microstructure analysis was examined using optical microscopy (Leica DM4000M) and scanning electron microscopy (Inspect S50). The EBSD study was performed on a Zeiss GeminiSEM 450 scanning electron microscope using 20 kV working voltage and 0.2 μ m step size for low magnification and 50 nm for high magnification. The samples were ground on SiC abrasive papers with gradations from 320 to 2400 of FEPA scale and polished with a solution of

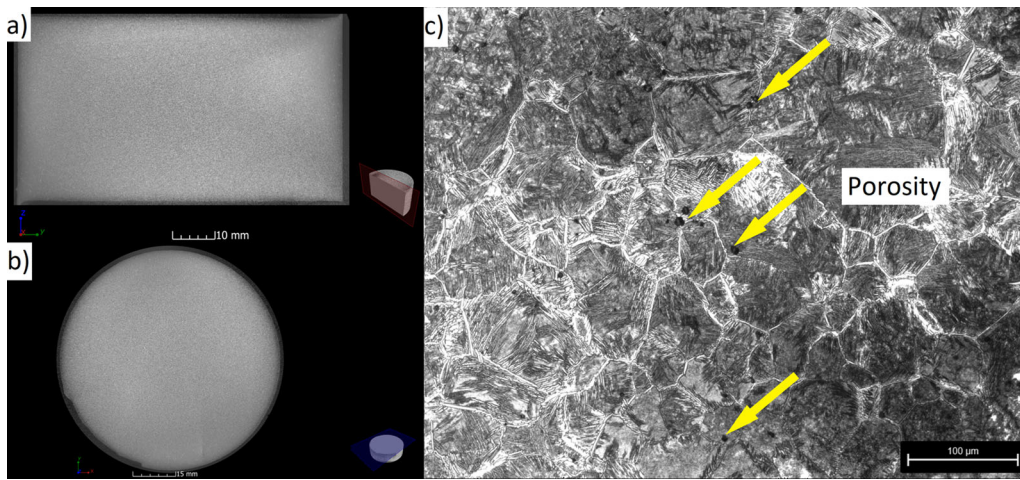


Fig. 1—Images of the internal structure of the Ti-5553 alloy compact obtained by CT scanning: (a) longitudinal section, (b) cross section, and (c) low-magnification microstructure with marked pores.

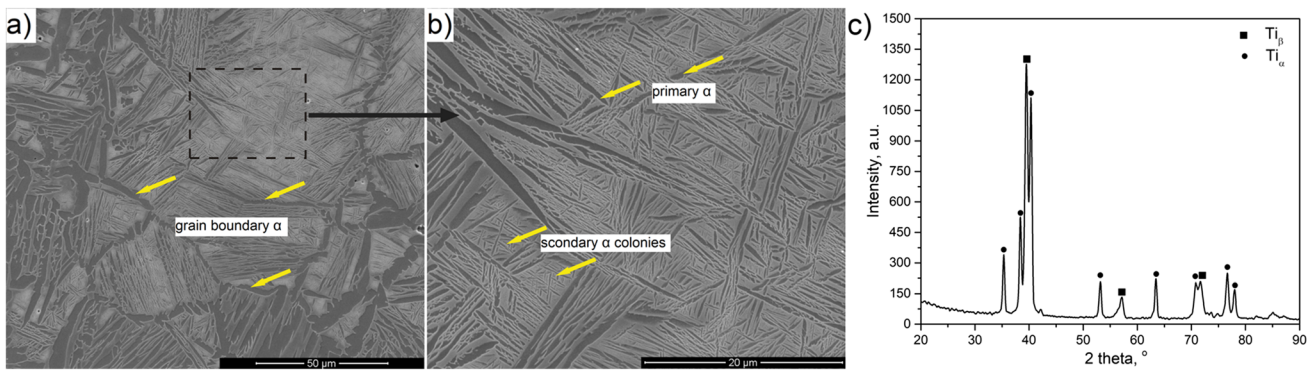


Fig. 2—(a) and (b) SEM-SE images of the initial microstructure, (c) XRD pattern of the Ti-5553 alloy compact.

hydrogen peroxide and colloidal silica suspension, then, if necessary, etched with Kroll's reagent consisting of 7 pct of HF, 14 pct of HNO₃, and 79 pct of H₂O.

Uniaxial tensile tests were carried out using a tensile testing module from Kammarth Weiss GmbH. The tests were carried out at a constant tensile speed of 0.005 mm/s at room temperature. The hardness test was carried out on Struers Duramin-40 with a load of 9.8 kN.

III. RESULTS AND DISCUSSION

A. Material Characterization After Hot Compacting

Qualitative evaluation of the internal structure of the compact was performed using non-destructive testing through CT scanning. The test was conducted at a resolution of 50 μm, capturing scans along the compact axis and perpendicular to it. Figures 1(a) and (b) display sample images of the internal structure obtained through CT scanning. Based on the scan analysis, the presence of internal defects such as cracks, discontinuities, or delamination within the tested compact volume was excluded. In addition, no pores larger than the

resolution used during the test were observed. Figure 1(c) presents a low-magnification microstructure image of the as-pressed Ti-5553 compact. Pores, indicated by yellow arrows, exhibited a spherical shape. They occurred individually rather than forming a pore network and were uniformly distributed throughout the material. The measured average pore size was $7 \pm 3 \mu\text{m}$. The obtained results confirm that the proposed method can be used to produce semi-finished products without internal defects that could have a negative impact on the deformation process.

The SEM microstructure of the as-pressed Ti-5553 alloy compact is presented in Figure 2. It exhibits distinct features, including thick α-phase plates positioned along the primary β-grain boundaries, lamellar colonies of α grains, and thin-needle-like α-phase precipitates dispersed within the β-phase matrix. This microstructure is typical of titanium alloys that undergo slow cooling from the β phase range (with the β-transus temperature of this alloy falling between 850 °C and 880 °C),^[21] which corresponds to the cooling conditions employed after hot pressing. Under such conditions, α-phase precipitation first occurs at the β grain boundaries in the form of elongated plates (known as grain

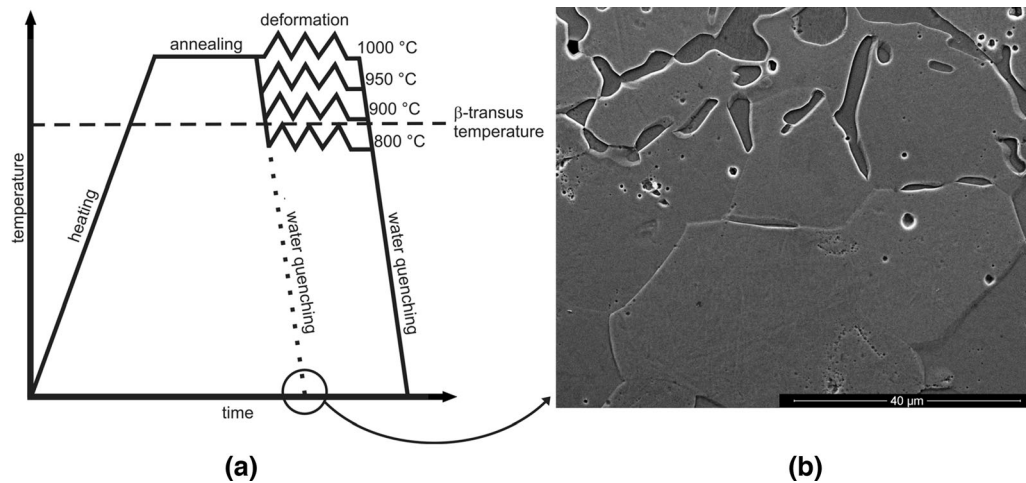


Fig. 3—(a) Schematic diagram of hot compression tests on the WUMSI simulator, and (b) SEM-SE microstructure after the annealing stage and water cooling.

boundary α phase, α_{GB}), followed by fine precipitates forming within the grains, which, upon growth, give rise to lamellar α grains (primary α phase). The presence of α_{GB} grains hinders the further growth of primary α grains within the original β grain, leading to the formation of enclosed primary α colonies. In addition, Figure 2(b) reveals the presence of fine secondary α phase colonies. Due to the substantial volume of α phase at room temperature, metastable β alloys like Ti-5553 cannot be cold formed as opposed to stable β alloys, which typically possess a microstructure composed mainly of equiaxed β grains and are commonly processed through cold rolling.^[22,23]

Figure 2(c) presents the XRD pattern of the Ti-5553 alloy compact. The results of the analysis align with the previous SEM observations. The XRD pattern shows distinct peaks corresponding to the hexagonal α phase and cubic β phase. No peaks associated with the individual alloying additives used in the powder mixture were observed. This indicates that the alloying additives were dissolved during the hot compacting process.

B. Flow Behavior

A schematic representation of the compression tests is shown in Figure 3(a). Furthermore, Figure 3(b) displays the SEM microstructure after the annealing stage followed by water quenching. The microstructure reveals the dissolution of a significant portion of the α phase grains and the growth of equiaxed β phase grains.

The flow curves of the Ti-5553 alloy compact, obtained from the hot compression tests, are presented in Figure 4. The selected range of hot compression parameters was intended to facilitate accurate constitutive modeling calculations and the construction of processing maps across a wide range of deformation parameters, both below and above the β -transus temperature. In addition, the parameter range was chosen to anticipate changes in temperature and strain rate during the planned hot-rolling process. All the curves exhibit a rapid increase in flow stress during the initial

stage of deformation. At temperatures of 1000 °C and 900 °C, for low strain rates (0.1 and 1 s^{-1}), the curves reach a peak stress and then plateau with further strain increase. For strain rates of 10 and 20 s^{-1} , the stress gradually decreases with increasing strain, known as the flow softening effect. This flow softening effect is more prominent at lower temperatures and higher strain rates. Irrespective of the strain rate, the flow stress decreases with increasing temperature. Similarly, as the strain rate decreases, the flow stress also decreases.

The non-linear flow behavior observed can be attributed to two phenomena. The rapid increase in stress at the beginning of the process is linked to the accumulation of dislocations, which hinder their movement within the existing grain boundaries.^[8] On the other hand, the flow softening effect is associated with the occurrence of DRV and DRX. As mentioned earlier, at high strain rates, a continuous softening curve is observed, which is directly influenced by the deformation heating resulting from the high deformation energy. Due to the low thermal conductivity of titanium, the heat generated during plastic deformation cannot be dissipated efficiently, leading to an increase in the material's temperature. This provides favorable conditions for DRX to become the primary softening mechanism.^[8,24] It is important to note that strain hardening occurs rapidly, while recovery or recrystallization requires both high temperature and time. Consequently, lower strain rates result in longer exposure to high temperatures, promoting a more stable material behavior. Conversely, at higher temperatures, the strain hardening effect diminishes quickly due to DRX, leading to early stabilization of the deformation process. During steady-state flow, the phenomena of strain hardening, recovery, and recrystallization compensate each other.

Figure 5 presents the peak stress and steady-state stress values for different test conditions. It is evident that at lower strain rates, the differences in peak stress values are relatively smaller for the curves obtained during deformation above the β -transus temperature. A

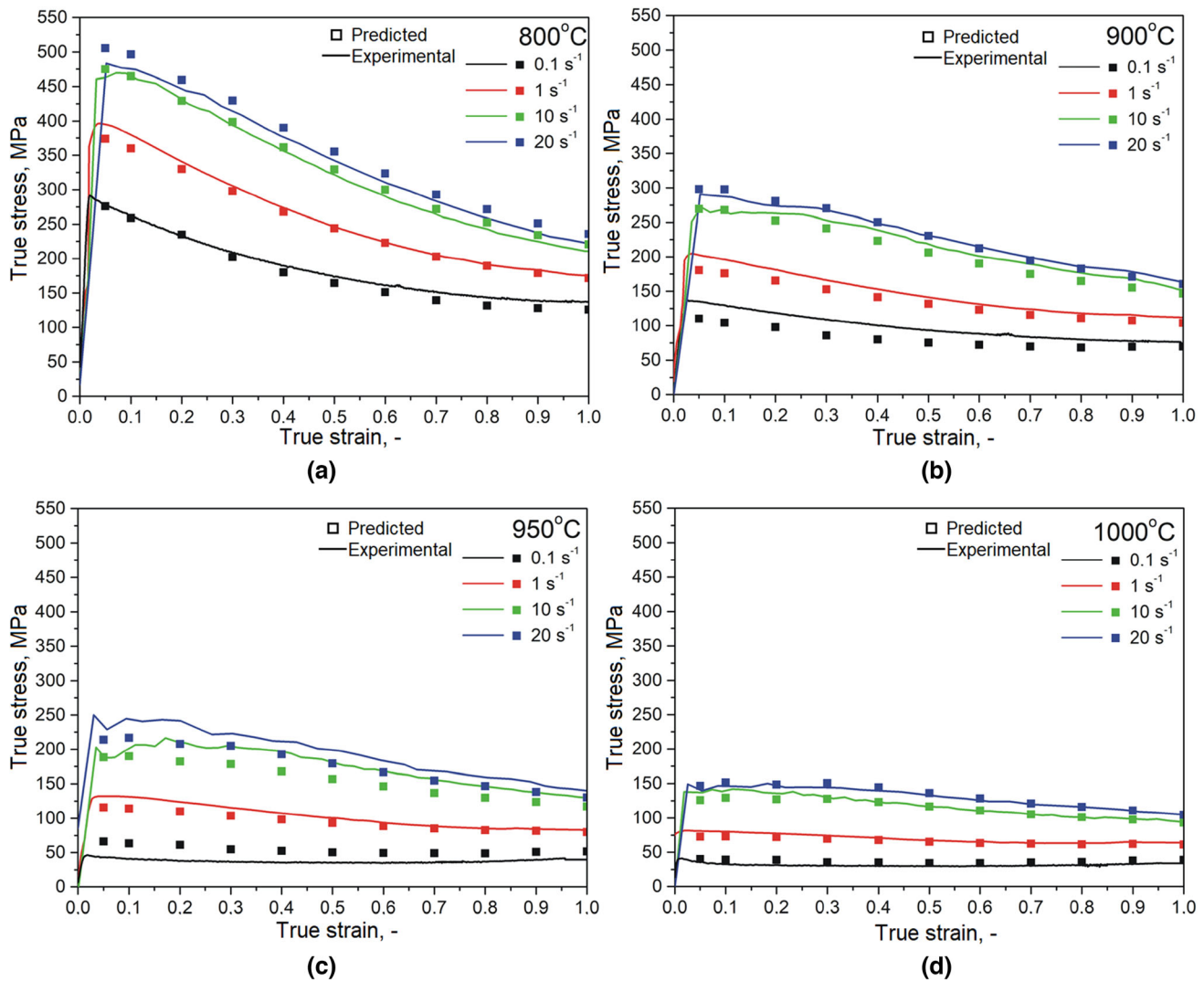


Fig. 4—Comparison of the predicted and experimental flow stress for the Ti-5553 alloy compact at deformation temperatures of (a) 800 °C, (b) 900 °C, (c) 950 °C, (d) 1000 °C.

similar trend is observed for the stress values during steady-state flow. However, a decrease in temperature below the β -transus temperature noticeably increases both the peak stress and steady-state stress values. On the other hand, for higher strain rates, there is a significant difference between the peak stress values obtained below and above the β -transus temperature, with a difference of approximately 200 MPa. In the case of steady-state flow, the stress decreases uniformly with increasing temperature for higher strain rates.

Compared to the results obtained for the Ti-5553 alloy through casting, as presented in the works,^[25,26] the obtained results in this study are similar or slightly higher. This difference could be attributed to variations in the initial microstructure and the higher oxygen content in the powder metallurgy-based alloy. Cast alloys generally have lower oxygen contamination compared to alloys produced *via* powder metallurgy. Oxygen content has a notable influence on flow stress. Previous studies by Wasz *et al.*^[27] and Xu *et al.*^[28] have demonstrated that oxygen increases flow stress,

especially at lower temperatures, and the effect is less significant as temperature increases. The effect of oxygen content in the range of 200 to 1500 ppm on hot deformation was investigated by Prasad and Seshacharyulu.^[29] They found that titanium alloys exhibit high sensitivity to changes in oxygen content, as evident from the analysis of processing maps. However, no obvious trend emerged from the studies presented. Titanium alloys produced through powder metallurgy are particularly susceptible to increased oxygen content. Liu *et al.*^[30] discussed the elevated oxygen content in TiAl alloys produced by powder metallurgy. They referred to the fact that the higher oxygen content leads to a significantly higher volume fraction of the α phase and to an increase in the thickness of the α phase lamellae. Therefore, the increased proportion of α -phase lamellae colonies can be observed in Figure 2, which shows the microstructure of the alloy after hot pressing. The authors of the work^[30] associate the increased volume of the lamellar α -phase with increased hardness and low elongation, but also which is great importance in hot

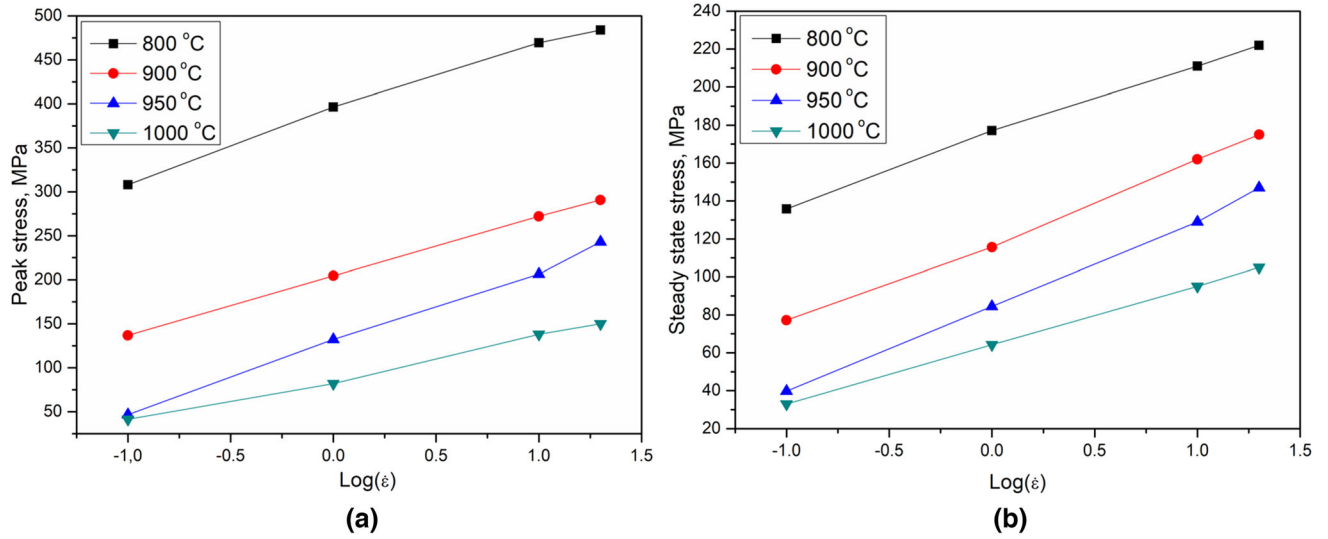


Fig. 5—Values of peak stress (a) and steady-state stress, (b) during hot compression tests of Ti-5553 alloy compact.

deformation with an increase in activation energy and flow stress. An interesting discussion on the effect of oxygen content was presented by Zhao *et al.*^[25] They concluded that high oxygen levels promote DRX as the primary mechanism of deformation. Oxygen is an interstitial element, so the dislocation motion is piled up due to the distortion of the lattice by the interstitial atom. The generation of dislocation tangles facilitates the nucleation of DRX grains. The higher the oxygen content, the more dislocation splicing occurs.

As mentioned previously, strain hardening occurs at the initial stage of the process, and as deformation continues, a reduction in stress is observed due to thermally activated phenomena. The flow behavior is influenced by changes in microstructure associated with DRX as the compression temperature increases. The nucleation and growth of new recrystallized grains, with a lower density of dislocations, contribute to a decrease in flow stress. Similarly, reducing the strain rate promotes DRX and leads to a reduction in flow stress. Therefore, an optimal combination of thermomechanical parameters can result in a fully recrystallized and fine-grained microstructure in titanium alloys after hot deformation.

C. Strain-Dependent Constitutive Equation and Deformation Activation Energy Map

The experimentally determined stress–strain relationship can be used to develop a constitutive equation, including the Zener–Hollomon parameter (Z) and the activation energy (Q). Determining these material characteristics aids in describing the behavior of the investigated material during deformation under different thermomechanical conditions, understanding the nature of microstructural changes, and predicting flow stress for varying process parameters. The relationship between strain rate, temperature, and flow stress can be expressed by an Arrhenius-type equation:

$$\dot{\epsilon} = A[\sinh(\alpha\sigma)]^n \exp(-Q/RT), \quad [1]$$

where ($\dot{\epsilon}$) is the strain rate, (σ) is the flow stress, (T) is temperature, (Q) is the activation energy, (R) is the universal gas constant, and (A), (α), and (n) are material constants. The Zener–Hollomon (Z) parameter, which is one of the most important indicators for considering theoretical problems in the field of hot deformation of metallic materials, can be described using the following equations:

$$Z = \dot{\epsilon} \exp(Q/RT) = A_1 f(\sigma), \quad [2]$$

$$Z = A_1 \sigma^{n_1}, \text{ where } : \alpha\sigma < 0.8, \text{ for low-stress levels,} \quad [3]$$

$$Z = A_2 \cdot \exp(\beta\sigma), \text{ where } : \alpha\sigma > 1.2, \text{ for high-stress levels,} \quad [4]$$

$$Z = A[\sinh(\alpha\sigma)]^n, \text{ for all conditions,} \quad [5]$$

where (A_1), (A_2), (β), and (n_1) are material constants, which can be calculated from the following equations:

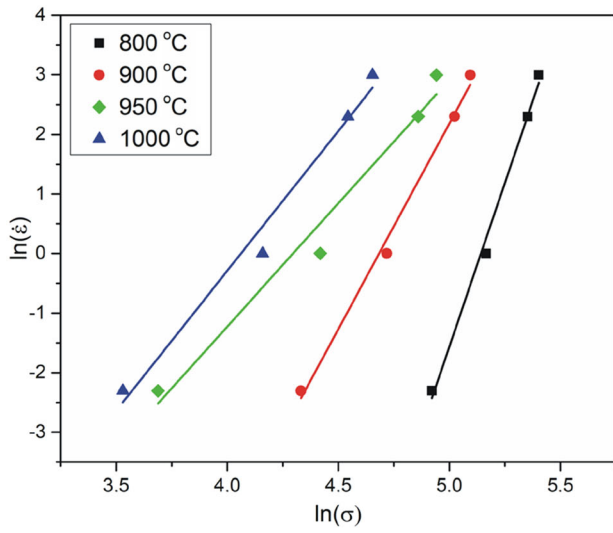
$$n_1 = (\partial \ln \dot{\epsilon} / \partial \ln \sigma)_T, \quad [6]$$

$$\beta = (\partial \ln \dot{\epsilon} / \partial \sigma)_T, \quad [7]$$

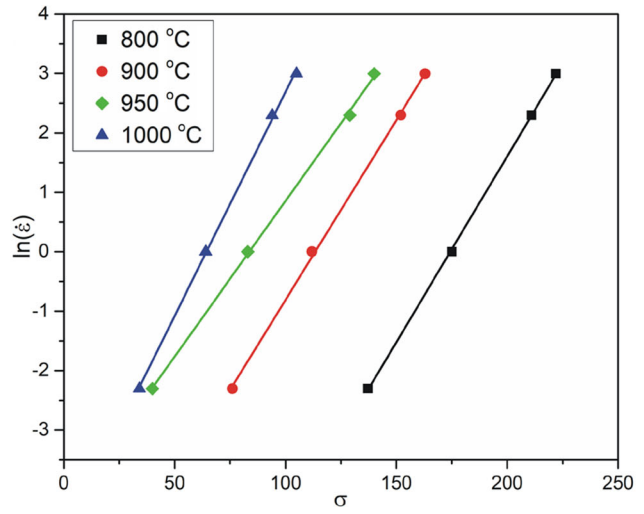
$$n = (\partial \ln \dot{\epsilon} / \partial \ln(\sinh(\alpha\sigma)))_T. \quad [8]$$

Then, to assess the hot deformability of the investigated material, the activation energy deformation (Q) was determined for a constant value of ($\dot{\epsilon}$), using the equation:

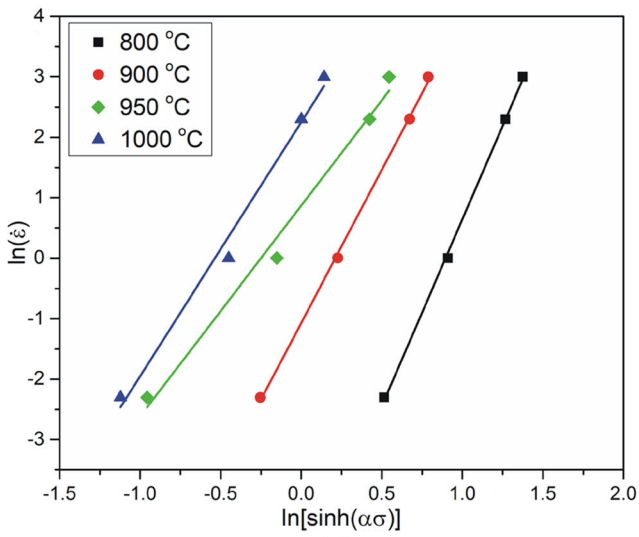
$$Q = R \cdot n \cdot |\partial \ln(\sinh(\alpha\sigma)) / \partial (1/T)|_{\dot{\epsilon}}. \quad [9]$$



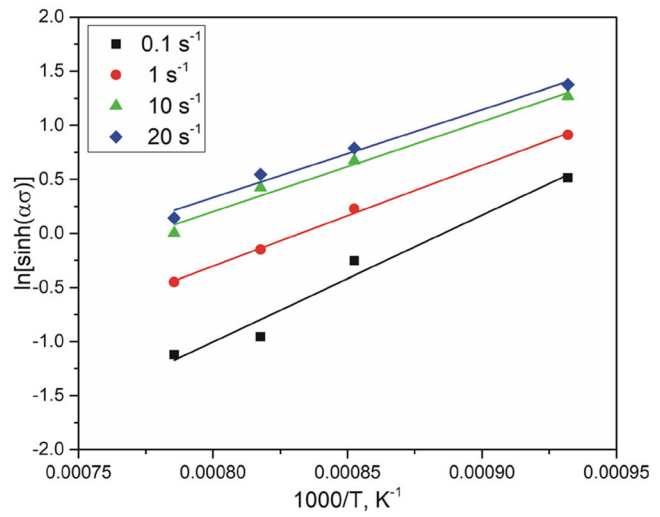
(a)



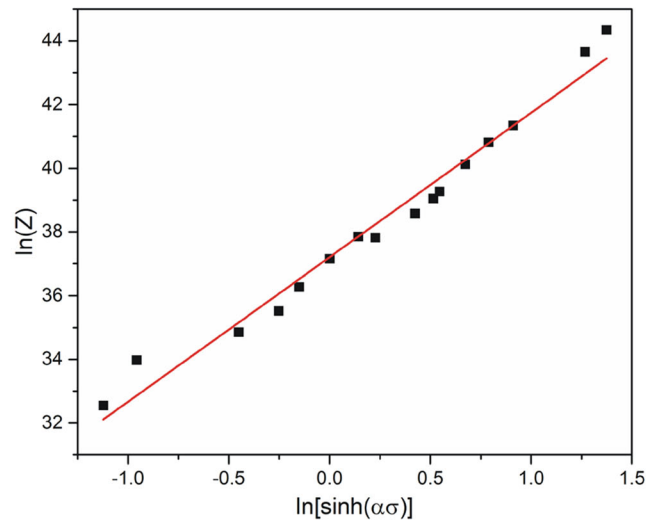
(b)



(c)



(d)



(e)

Fig. 6—Relationship between (a) $\ln(\dot{\epsilon})-\ln\sigma$, (b) $\ln(\dot{\epsilon})-\sigma$, (c) $\ln(\dot{\epsilon})-\ln[\sinh(\alpha\sigma)]$, (d) $\ln[\sinh(\alpha\sigma)] - 1/T$, (e) $\ln(Z)-\ln[\sinh(\alpha\sigma)]$ for Ti-5553 alloy compact.

The Z parameter and the average value of the activation energy (n) were determined based on the data obtained in the hot compression tests performed in a wide range of strain rates and temperatures. Therefore, Eq. [5] is used in the calculations, which is applied to a wide range of stress values. The mean values of the material constants were determined based on the linear regression of the relationship between $\ln(\dot{\epsilon})$ and $\ln(\sigma)$, σ and $\ln[\sinh(\alpha\sigma)]$, which are presented in Figure 6.

For known material constants (Table I), it is possible to calculate the average Q value, using Eq. [9]. For the Ti-5553 alloy compact, the average Q value was

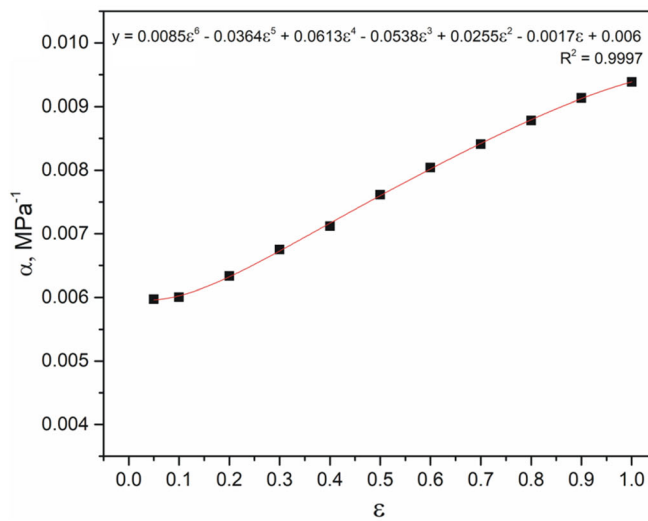
Table I. Material Constants and Average Activation Energy for the Ti-5553 Alloy Compact

N_1	β	α (Mpa ⁻¹)	n	A	Q (kJ/mol)
6.684	0.062725	0.009385	4.733	1.437×10^{16}	368.84

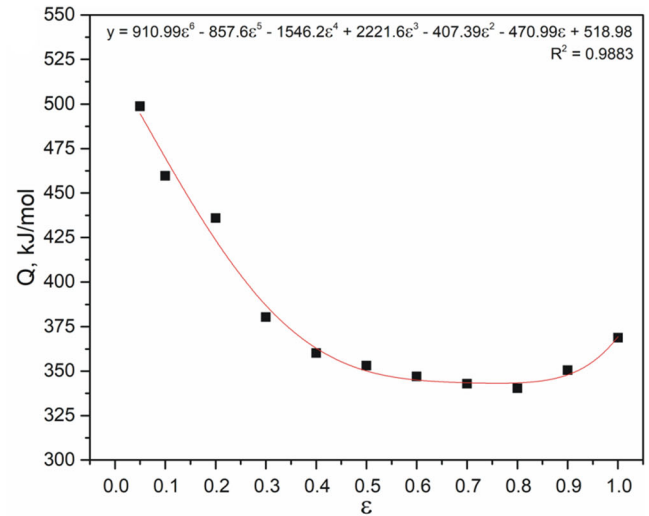
368.84 kJ/mol. The Arrhenius-type constitutive equation that describes the behavior of the Ti-5553 alloy compact in the hot deformation process can be expressed as follows:

$$\dot{\epsilon} = 1.437 \times 10^{16} [\sinh(0.009385\sigma)]^{4.733} \exp(-36884/RT). \quad [10]$$

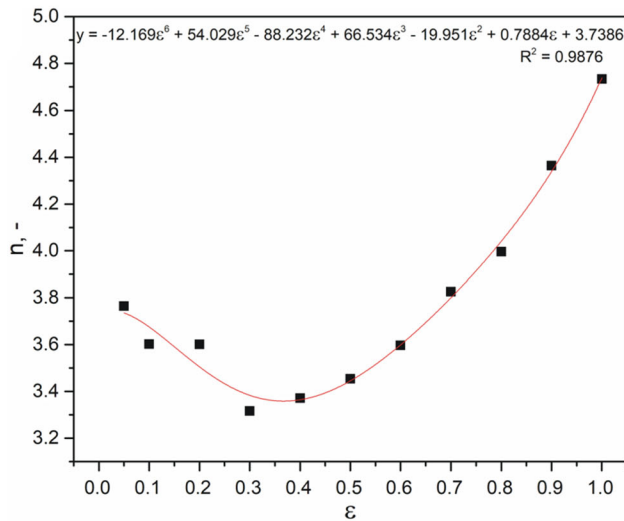
Based on Eq. [10], the value of the Zener–Hollomon parameter can be determined for variable deformation conditions (temperature and strain rate). Figure 6(e) shows the value of $\ln Z$ as a function of $\ln[\sinh(\alpha\sigma)]$, along with a linear regression of this relationship. The stress increases proportionally to the value of the Zener–Hollomon parameter, so the distribution becomes linear. The linear regression correlation coefficient is $R^2 = 0.975$, which confirms the high accuracy of the constitutive equation that describes the behavior



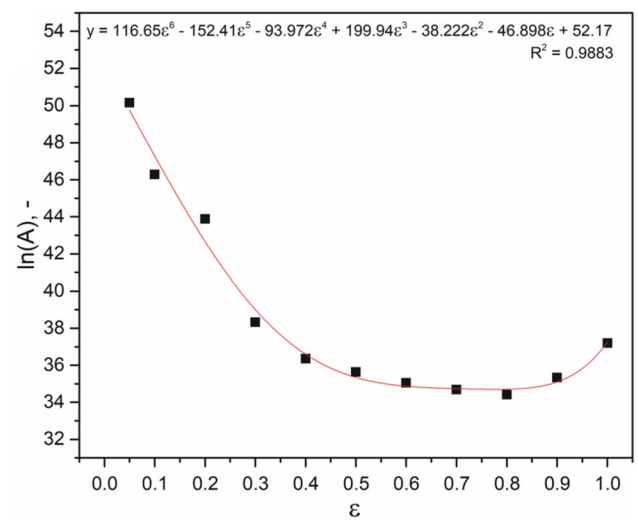
(a)



(b)



(c)



(d)

Fig. 7—Relationships between the actual deformation value and material constants (a) α , (b) Q , (c) n , and (d) $\ln(A)$ for the molded part made of Ti-5553 alloy.

of Ti-5553 alloy compact during high-temperature deformation.

For a variable value of the Z parameter, the predicted stress value can be calculated from the equation:

$$\sigma = 1/\alpha \ln \left\{ (Z/A)^{\frac{1}{n}} + \left[(Z/A)^{\frac{2}{n}} + 1 \right]^{\frac{1}{2}} \right\}. \quad [11]$$

Observation of the flow curves indicated that with increasing strain, the stress decreases, especially with a lower deformation temperature, which has to be considered during the calculation of the predicted flow stress. Therefore, the material constants were determined for the range of $\varepsilon = 0.05$ – 1.0 . The relationship between material constants and strain value can be adjusted using polynomials. The parameters α , Q , n , and $\ln(A)$ were written as a sixth-degree polynomial as a function of strain according to Eq. [12] and shown in Figure 7.

$$\begin{cases} A = B_6\varepsilon^6 + B_5\varepsilon^5 + B_4\varepsilon^4 + B_3\varepsilon^3 + B_2\varepsilon^2 + B_1\varepsilon + B_0 \\ Q = C_6\varepsilon^6 + C_5\varepsilon^5 + C_4\varepsilon^4 + C_3\varepsilon^3 + C_2\varepsilon^2 + C_1\varepsilon + C_0 \\ n = D_6\varepsilon^6 + D_5\varepsilon^5 + D_4\varepsilon^4 + D_3\varepsilon^3 + D_2\varepsilon^2 + D_1\varepsilon + D_0 \\ \alpha = E_6\varepsilon^6 + E_5\varepsilon^5 + E_4\varepsilon^4 + E_3\varepsilon^3 + E_2\varepsilon^2 + E_1\varepsilon + E_0 \end{cases} \quad [12]$$

To assess the precision of the developed model, the calculated stress values were compared with the experimental flow stress values, as shown in Figure 4. The predicted flow stress is in good correlation with the experimental values, which proves that the constitutive equation predicts the behavior of Ti-5553 alloy compact during hot deformation accurately.

Furthermore, Figure 8 shows the correlation between the experimental and calculated stress values. In addition to the correlation coefficient R^2 , the average absolute relative error (AARE) was calculated using the formula:

$$\text{AARE} = 1/N \sum_{i=1}^N |E_i - P_i/E_i| \times 100, \quad [13]$$

where E_i is the experimentally measured value of the flow stress and P_i is the calculated value of the flow stress. The calculated values of R^2 and AARE in the range of true strain of 0.1–1 were 0.9775 and 9.63 pct, respectively. This shows that the developed constitutive model and the calculated material constants well describe the relationships between flow stress, temperature, strain rate, and strain for the investigated material.

The deformation activation energy is an important parameter that provides information on the mechanisms related to the evolution of the microstructure during hot deformation. It is necessary to analyze not only its average Q value but also the distribution depending on the adopted deformation conditions.

Figure 9 shows a map of the deformation activation energy (Q) as a function of strain rate and temperature for Ti-5553 alloy compact, for $\varepsilon = 1.0$. The

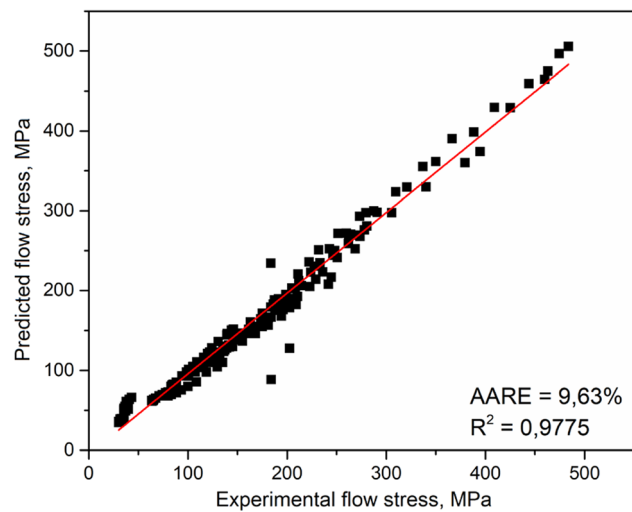


Fig. 8—Correlation between the experimental and the calculated flow stress for the Ti-5553 alloy compact.

deformation activation energy increases with increasing temperature and decreasing strain rate. A similar trend was previously observed for other β titanium alloy (Ti-15-3)^[31] and the casted Ti-5553 alloy.^[25] The Q values within the applied range of process parameters range from approximately 240 to 540 kJ/mol. The microstructure of the deformed material has a significant impact on the activation energy value. At the temperature below β -transus, the expected mechanism of microstructure evolution is DRV. The kinetics of DRV are associated with dislocation sliding and climbing along grain boundaries, which was shown by Chuan and Liang.^[32] In this case, the energy required to activate this process is closer to the energy of titanium self-diffusion in the β phase (135–153 kJ/mol).^[33] The high Q values obtained in the temperature range from 900 °C to 1000 °C indicate that the DRX is the dominant mechanism for microstructure evolution. Areas exhibiting relatively uniform activation energy, observed at lower strain rates, are preferred for selecting the most favorable conditions for hot deformation. However, to validate the occurrence of these phenomena, a microstructural analysis after deformation should be conducted.

D. Processing Maps

The processing maps developed based on the Dynamic Material Modeling (DMM) method are a useful tool for optimizing deformation parameters and prediction of the dominant mechanism of microstructure evolution during hot forming. The development of processing maps follows the approach initially proposed by Prasad *et al.*^[34] The calculation methodology has been extensively described by the authors in previous publication^[13] providing a detailed understanding of the process.

Based on the stress–strain data and the DMM model, processing maps for the Ti-5553 alloy compact were developed for true strain values of 0.2, 0.6, and 1.0, as

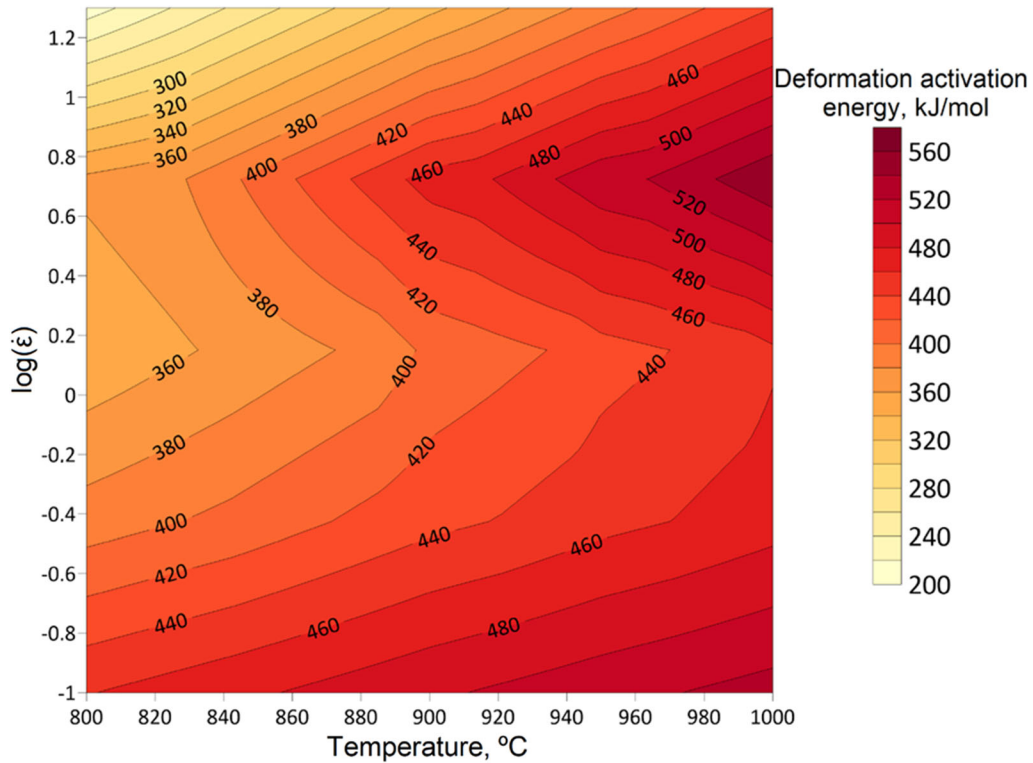


Fig. 9—The deformation activation energy map of the Ti-5553 alloy compact for the true strain of 1.0.

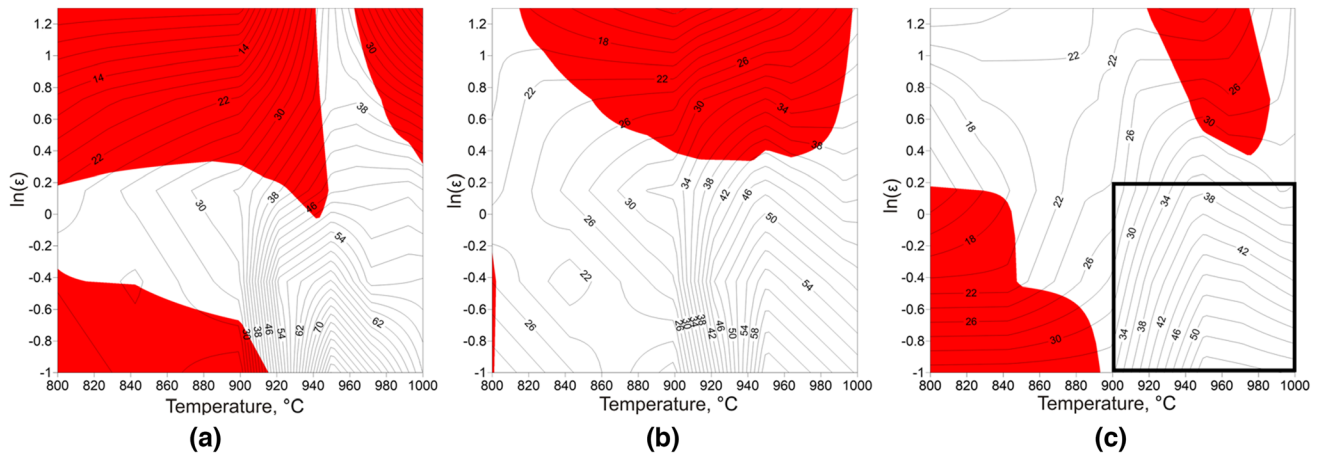


Fig. 10—Processing maps for Ti-5553 alloy compact developed for a true strain of (a) 0.2, (b) 0.6, and (c) 1.0.

shown in Figure 10. The isolines represent the efficiency of the power dissipation coefficient η expressed in percentage. The areas of flow instability are highlighted in red. Figure 10(a) represents the processing map for a relatively low true strain value of 0.2, corresponding to the initial stage of deformation characterized by a significant increase in stress. In this region, there is a state of flow instability and low values of the parameter η are observed for most combinations of temperature and strain rate. However, as the deformation progresses, the areas of instability decrease, indicating the occurrence of microstructural evolution through mechanisms such as DRV or DRX.

On the other hand, at the early stage of deformation for temperatures ranging from 900 °C to 1000 °C, high values of the parameter η are observed particularly for low strain values. The isolines on the processing map are closely spaced, indicating a dense distribution. This temperature range is related to the ongoing phase transformation, which for Ti-5553 alloys begins approximately at 850 °C.^[26] The increase in η in these conditions can be attributed to significant microstructural changes, including the dissolution of remaining α -phase grains (Figure 3(b)) and the growth of β -phase grains. As the true strain value increases to 1.0, the area

of flow instability diminishes, and the distribution of isolines becomes more uniform.

The processing map for the true strain of 1.0 is shown in Figure 10(c). The area of flow instability for high strain rates has decreased and is visible only for the temperature range from 920 °C to 990 °C. Additionally, for strain rate values of 0.1–2.0 s⁻¹ and temperatures below the β -transus, a second instability area is observed. Combinations of process parameters covering the areas mentioned above should be avoided when designing hot-forming processes of this type of alloy to minimize the risk of microstructural defects.

The region characterized by a high value of the η parameter is observed within the range of strain rates of 0.1 to 2.0 s⁻¹ and temperatures of 890 °C to 1000 °C. The parameter η within this range exhibits values ranging from 34 to 54 pct, with the maximum value obtained at the combination of parameters: 960 °C and 0.1 s⁻¹. This suggests that DRX is expected to occur prominently in this region. Furthermore, it is worth noting that the distribution of isolines for the energy dissipation efficiency parameter is relatively uniform within this range. This uniform distribution suggests that the material flow remains in a steady-state during this stage of deformation, which is consistent with the observed flow curves.

A processing window with a relatively wide range of parameters has been defined for low strain rates (0.1–2.0 s⁻¹) and temperatures in the range from 900 °C to 1000 °C. This selected region is characterized by a favorable efficiency of the power dissipation coefficient and a uniform distribution of isolines. However, the combination of parameters: 800–920 °C/2.0–20 s⁻¹, although free of flow instability, was not chosen as a potential processing window. This decision was based on the analysis of processing maps for lower true strain values, which indicated a high risk of flow instability and potential microstructural defects within this region. In addition, this region exhibited a low value of the η parameter. It should be noted that this does not imply that deformation of the test alloys at high strain rates is impossible. Tests conducted for titanium alloys with a different chemical composition, but produced using the same method,^[13] have shown that it is possible to locate the processing window also for high strain rates but assuming that the process will be carried out at a sufficiently high temperature. In the case of near- β titanium alloys, the deformation process should be carried out above the β -transus temperature. Titanium has relatively low thermal conductivity. Nemat-Nasser *et al.*^[35] showed that the increase in temperature during deformation can reach to 80 °C. Therefore, it can be assumed that deformation of the Ti-5553 alloy compact at a temperature of 1000 °C and with a sufficiently high strain value would help avoid flow instability.

E. Microstructural Validation

After the hot compression test, each deformed sample was water quenched to maintain the microstructural state immediately after deformation. This step enabled an examination of the influence of thermomechanical

parameters on the evolution of the microstructure. Furthermore, the analysis of the microstructure in the post-deformation state served as a validation of the processing maps developed earlier. Therefore, particular attention was given to the combinations of parameters where the occurrence of flow instability was identified, as well as those that fell within the designated processing window.

Figure 11 shows chosen microstructures of Ti-5553 alloy compact deformed at different thermomechanical parameters. Figure 11(a) and (b) shows microstructures of samples deformed at a temperature of 800 °C. In this variant, the deformation took place below the β -transus temperature. Therefore, after annealing at 1000 °C, the samples were cooled to the deformation temperature relatively slowly and nucleation and growth of new α grains took place.

Regardless of the strain rate value, several distinctive microstructure features are evident in the Ti-5553 alloy compact deformed at a temperature of 800 °C. The α grains exhibit elongation along the flow direction and partial fragmentation. In addition, larger, globular α -phase grains can be observed. The mechanism behind α phase fragmentation, referred to as globularization or spheroidization, has been elucidated by Semiatin *et al.*^[36] Plastic deformation results in the accumulation of dislocations and the formation of substructures or shear bands within the α -phase plates. Consequently, HAGBs form in these regions, leading to grain separation and spheroidization. The microstructures obtained at strain rates of 0.1 and 1 s⁻¹ (Figures 11(a) and (b)) correspond to parameter sets that were identified as potentially unsafe based on the processing map analysis. Flow localization regions were observed, which could potentially give rise to the formation of adiabatic shear bands. The presence of microstructural inhomogeneities can also contribute to a decrease in mechanical properties.

Figure 11(c) shows the microstructure of the sample compressed at 950 °C/0.1 s⁻¹. In this case, the deformation process was carried out above the β -transus temperature, leading to a significant increase in the β phase content. The α grains are oriented in the flow direction, and there is a higher number of equiaxed α grains, indicating a more pronounced α phase globularization compared to the microstructure obtained at 800 °C. Figure 11(d) shows the microstructure of the deformed samples at a temperature of 1000 °C and a strain rate of 1 s⁻¹. Observations reveal a significant enlargement of the β phase grains. The α phase exhibits a smaller volume fraction compared to the microstructure obtained at 950 °C, with α grains present in both spheroidal and plate-like forms. Dehghan-Manshadi and Dippenaar^[37] demonstrated that deformation in the temperature range above the β -transus temperature, coupled with a relatively high true strain, not only promotes phenomena such as α phase globularization or DRX but also induces extensive growth of the β phase grains.

These sets of parameters, determined using the DMM method, have been identified as the most favorable for the deformation of the Ti-5553 alloy compact.

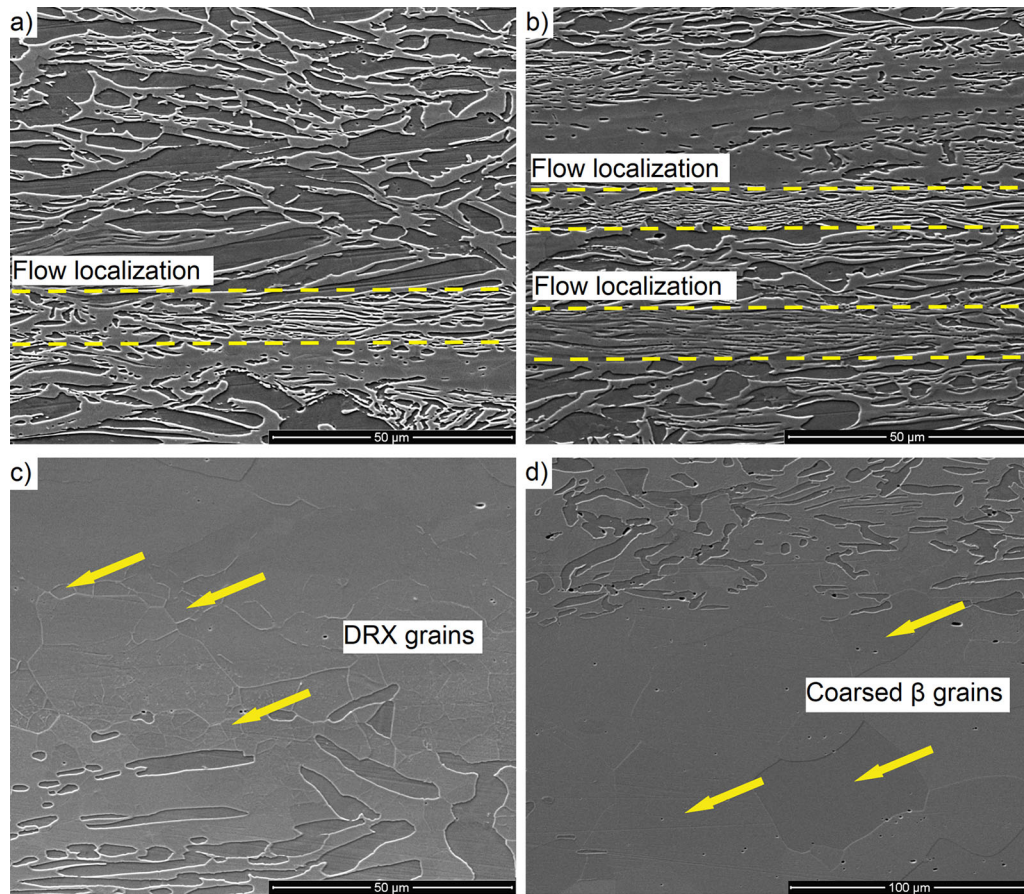


Fig. 11—SEM-SE microstructures of Ti-5553 alloy compact hot compressed at (a) 800 °C/0.1 s⁻¹, (b) 800 °C/1 s⁻¹, (c) 950 °C/0.1 s⁻¹, (d) 1000 °C/1 s⁻¹.

Consequently, in addition to the aforementioned spheroidal α phase grains, relatively small equiaxed β phase grains are also present, indicating the occurrence of DRX under these conditions. These observed microstructural changes validate the earlier findings derived from the analysis of the processing maps. The high value of the η parameter is attributed to the intense microstructural transformations, in this case identified as DRX.

The analysis of the microstructure of the samples deformed in the hot compression tests allowed for the validation of the results obtained based on the DMM method. It was found that the processing maps developed for the Ti-5553 alloy accurately describe its behavior during hot deformation within the temperature and strain rate ranges employed in the tests. The correlations previously established between the distribution of the η parameter, and the regions of flow instability successfully predict the microstructural changes occurring during deformation under the proposed thermomechanical conditions.

F. Finite Element Modeling

The FEM analysis was performed using QForm v.9.0.20.36 software to determine favorable parameters and conditions for the hot-rolling process. The

simulation was conducted within the temperature limits specified by the processing window identified through the DMM method. Flow curves obtained from plasticity tests on the WUMSI simulator were used to describe the material's rheology during the modeling. Additional material characteristics relevant to its behavior during hot deformation were derived from separate tests and implemented into the simulation.

Differential Scanning Calorimetry (DSC) was used to determine the specific heat, and thermal diffusivity tests were performed using the Laser Flash Apparatus (LFA) flash method. Based on the results of these tests as well as density measurement, the thermal conductivity value was calculated. Figure 12 summarizes the results of tests and calculations of the mentioned coefficients in the temperature range of 700 °C–1050 °C.

Nonlinear behavior of changes in thermal properties with temperature was observed. A decrease in thermal diffusivity is observed at a temperature of about 900 °C. On the other hand, the decrease in the C_p and λ coefficients occurs at 750 °C. This trend is most likely a result of the remodeling of the crystallographic structure during the β -transus. From the temperature range of 850 °C–900 °C, which corresponds to the end of the phase transformation, a linear decrease in specific heat and thermal conductivity is observed with increasing temperature.

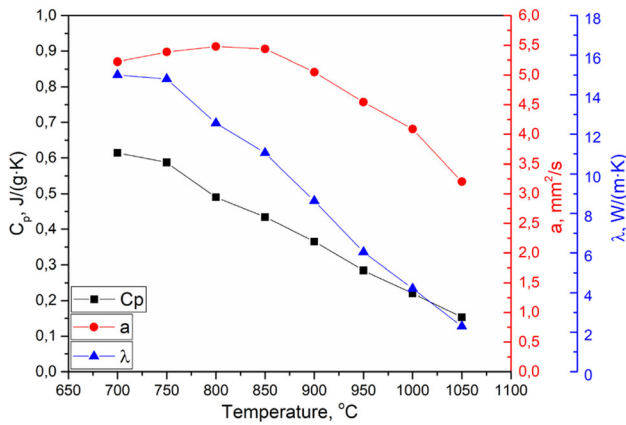


Fig. 12—Changes in thermal properties as a function of temperature for a Ti-5553 alloy compact. C_p specific heat, a thermal diffusivity, λ thermal conductivity.

Understanding thermal parameters is crucial for accurate modeling of hot deformation processes. This includes determining the temperature distribution within the material, modeling heat exchange between the tool and the environment, and analyzing the efficiency of converting plastic deformation work into heat. It is important to use data specific to the alloy being studied, as implementing data from literature for alloys with different compositions or production methods can lead to inaccuracies in the modeling of phenomena during hot deformation. In addition, an analysis of the literature has shown that there is currently a lack of comprehensive data on the thermal properties of the Ti-5553 alloy, such as specific heat or thermal conductivity, in terms of its hot-forming temperature.^[38] Existing literature mostly provides information on the thermal properties of titanium alloys at room temperature^[39] or within the range of 20 °C to 700 °C, primarily focused on machining and process modeling.^[40]

The determination of the friction coefficient value is crucial in accurately estimating the distribution of stress and strain intensity during the simulation of hot deformation processes. It directly influences the force required for the deformation process, enabling the selection of appropriate equipment. Furthermore, the friction coefficient plays a significant role in assessing tool wear. Hence, it was necessary to determine the friction coefficient under the specific conditions of hot processing. For this purpose, a ring compression test was carried out. A constant true strain value of 0.3 was assumed, and the height of the sample after compression was verified by manual measurement.

To estimate the friction coefficient, a series of FEM numerical analyses were performed using previously developed material characteristics. Simulations were conducted to replicate the conditions of the ring compression test. Each simulation incorporated a different value of the friction coefficient, ranging from 0.0 to 0.8 with an interval of 0.1. The dimensions of the compressed rings were then extracted from the simulation results. By comparing the simulated dimensions with the actual height of the deformed ring and

systematically adjusting the friction coefficient values in the software, an estimated friction coefficient of 0.28 was determined for the Ti-5553 alloy under the studied conditions.

The FEM numerical analysis of the hot-rolling process was conducted using previously established material characteristics and by simulating the technical conditions specific to the rolling mill on which the hot rolling was planned. This approach allowed for the verification of the modeling results against experimental data. The rolling process was simulated in 7 consecutive passes, employing both oval and square-shaped rolls. After each pass, the material was rotated by 90 deg to ensure a uniform deformation. Roller models were developed based on technical drawings and implemented in the QForm software. The feedstock model had a square cross section with a side length of 30 and 40 mm length. The calculations assumed a roller temperature of 20 °C and a material temperature of 1000 °C. According to the processing maps developed for the Ti-5553 alloy compact, this temperature will avoid deformation in the region of instability, particularly in the initial stage.

The distributions of several parameters, including temperature, effective stress, mean stress, and plastic strain, were analyzed during the consecutive simulations of the hot-rolling process. These parameters were monitored along the longitudinal section of the material in each pass. The results of the simulations were presented to allow for an evaluation of the changes in parameter distribution in different regions. The cross section to be observed was chosen so that the area of material before entry into the rolling zone, the intermediate region between the rollers, and after exiting the rolling zone could be seen. The results of the FEM simulation of a hot-rolling process for passes sixth and seventh are shown in Figure 13.

During the analysis of the simulation results, it was observed that due to contact with the tools, the material experienced the most cooling near the surface. On the other hand, a local increase in temperature was observed in the center of the cross section, which was a result of the conversion of plastic deformation work into heat. In the sixth pass, the material temperature is dropped to about 800 °C (Figure 13(a)), which caused a significant increase in effective stress (Figure 13(b)). Consequently, it is expected that continuing the rolling process without reheating the material at this stage may lead to overcooling and a significant decrease in plasticity, and even failure. Based on these findings, it was necessary to incorporate a reheating step at the final stage of rolling, specifically before the sixth or seventh pass. Therefore, the process was modified to include reheating the feedstock to 1000 °C prior to the last pass, which provided the best results. The results presented in Figure 13 take into account the reheating operation at this stage of the process.

The effective stress distribution, as shown in Figure 13(b), exhibits common characteristics regardless of the pass. It reaches maximum values in the region between the rollers and shows a locally elevated stress at the initial contact point between the metal and the rolls.

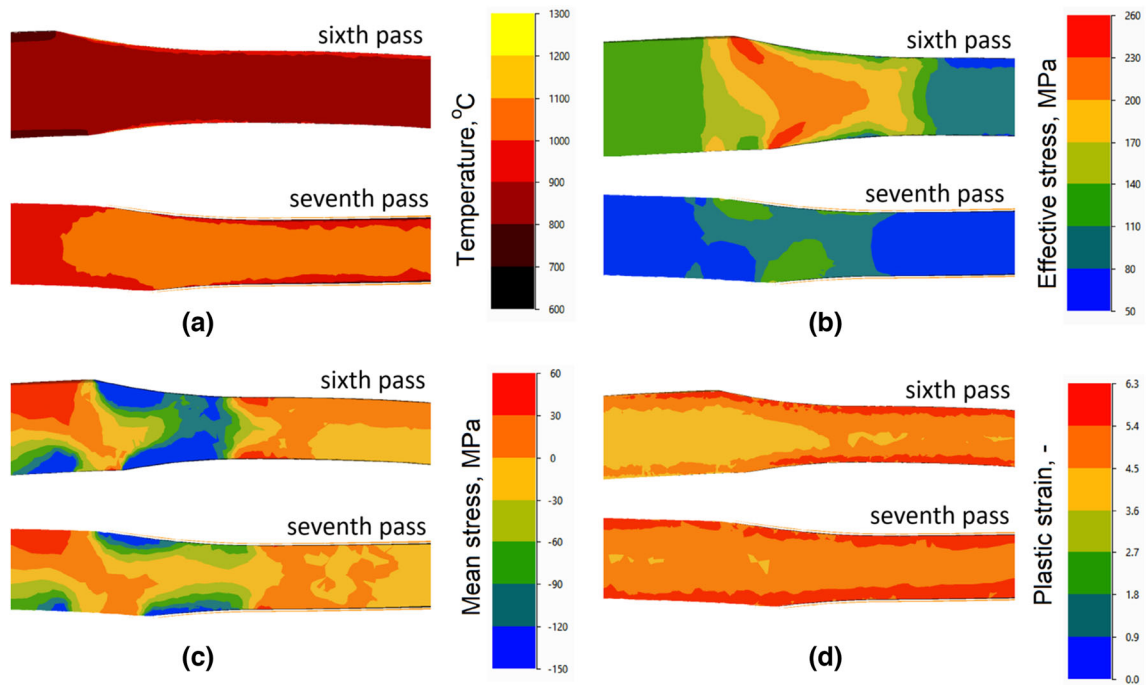


Fig. 13—FEM simulation results of the hot-rolling process of Ti-5553 alloy compact. Distribution of (a) temperature, (b) effective stress, (c) mean stress, (d) plastic strain.

As the material is pulled through the rollers, the effective stress distribution takes on the shape of a wedge elongated in the rolling direction. Throughout passes 1 to 6, the gradual decrease in material temperature results in an increase in effective stress. The range of effective stress values observed during simulations ranged from 230 to 260 MPa. However, with the reheating of the material before the seventh pass, a significant decrease in the value of effective stress is observed. Compressive stresses dominate the distribution (Figure 13(c)), particularly near the contact surface between the material and the tool. Small tensile stresses were observed before the material entered the zone between the rollers and after exiting this zone.

The distribution of plastic strain (Figure 13(d)) on the cross section of the rolled rod varied depending on the shape of the rolls used for deformation. When the material passed through rolls with oval cross sections, a uniform distribution of plastic strain values was observed throughout the rod. However, deformation in square rollers resulted in higher values of plastic strain in the region near the material rollers' interface. This effect can be attributed to the 90° rotation of the rod after each pass, causing a reduction in height and deformation dictated by the shape of the square rollers. After the final pass, which resulted in a rod with a circular cross section, a higher strain intensity was recorded near the surface, while a slightly lower value was observed in the middle part of the rod (Figure 13(d)).

The simulation of the hot-rolling process for a Ti-5553 alloy compact confirmed the feasibility of implementing this process under the proposed conditions. It was determined that to ensure the successful

completion of the rolling process, it is necessary to reheat the material after the sixth pass. This adjustment ensures the desired temperature and enhances the plasticity of the material, thereby avoiding potential failures and achieving the desired final product.

G. Verification by Hot Rolling

To verify the previously developed parameters for the hot deformation of Ti-5553 alloy produced from a mixture of elemental powders, a rod hot-rolling test was carried out. The parameters were developed based on the findings of previous studies, including DMM analysis and FEM modeling. These studies not only confirmed the feasibility of hot rolling without failure but also determined the optimal deformation temperature and conditions for the process. The rolling test was a verification of the accuracy of the thermomechanical parameters for the hot forming of the Ti-5553 alloy, which were derived from the results of the earlier investigations.

A sample with a square cross section of 30 mm sides and a length of 65 mm was cut from the compact. The sample was then heated to 1000 °C and subjected to rolling in seven consecutive passes. After the sixth pass, the material cooled to the point that further rolling was not possible. The process was stopped, and the rod was reheated to 1000 °C before undergoing the final pass to achieve the desired diameter. A rod with elliptical cross section with a long axis length of 10.40 mm and a short axis length of 9.20 mm was obtained. A similar rolling technique using the same rolling mill was used by Wojtaszek *et al.*^[41] During the hot rolling of the dual-phase Ti-6Al-4V alloy, which has an

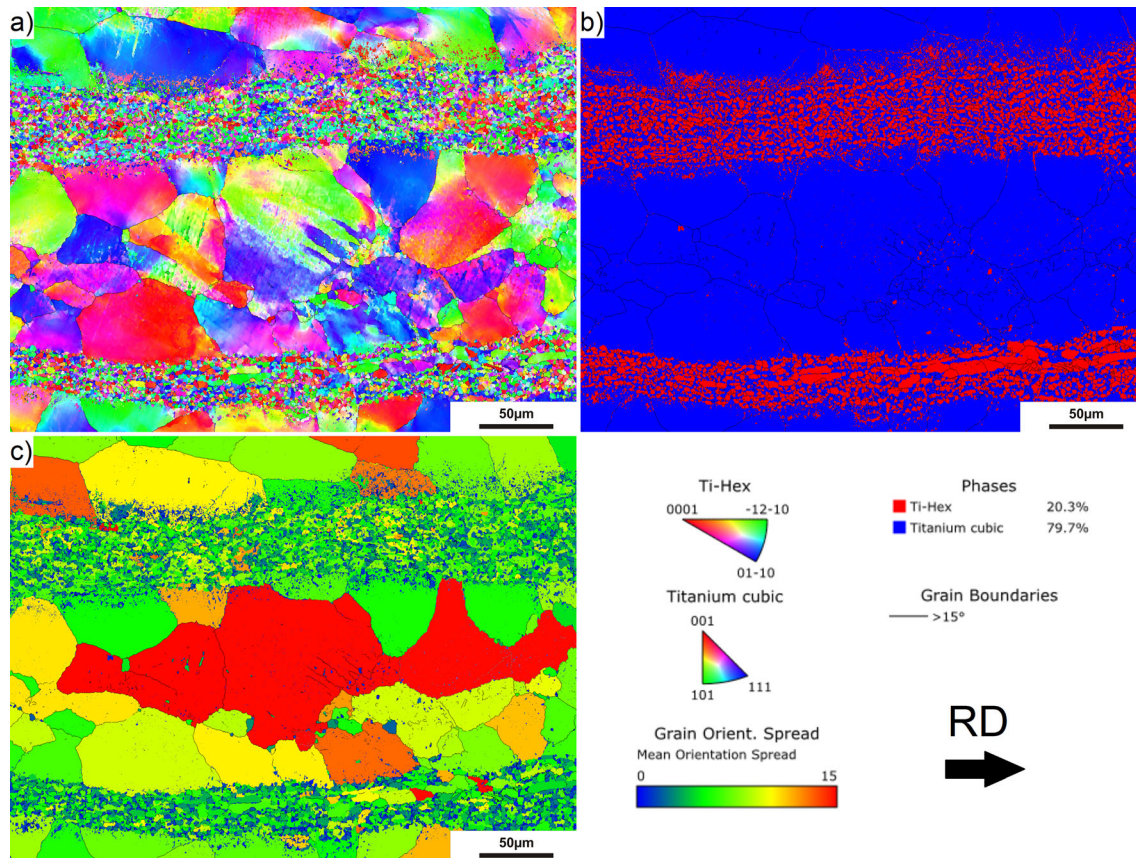


Fig. 14—EBSD maps of hot-rolled Ti-5553 compact; (a) IPF map; (b) phase map; (c) GOS map.

approximately 100 °C higher phase transformation temperature, the material had already cooled down after 5 passes to the point that continuing rolling without failure was not possible. Since β titanium alloys maintain higher deformability over a wider temperature range compared to dual-phase titanium alloys, the material under study was able to be hot rolled in a single sequence of operations in 6 passes.

Figures 14, 15, and 16 present the results of EBSD analysis of the Ti-5553 alloy compact after hot rolling. Figure 14 shows the general character of the microstructure after hot deformation, where fine spherical grains of the α phase are visible, alternating with elongated grains of the β phase. The phase distribution map (Figure 14(b)) confirms the banded microstructure. Compared to the initial microstructure, the proportion of the β phase significantly increased after rolling, accounting for nearly 80 pct. Figure 14(c) shows the grain orientation spread (GOS) map. GOS represents the average deviation of orientation for all points within a grain.^[42] The deformed grain exhibits a higher GOS value compared to a grain after recovery or DRV. It is generally accepted that the GOS value for recrystallized grains is less than 2°, while a GOS value greater than 7.5° is characteristic of a deformed grain. When the GOS value falls within this range, the grain is considered to be after DRV.^[43,44] Analyzing the GOS map, it can be observed that deformed or post-DRV grains dominate in the β phase band. However, on the prior β grain

boundaries, DRV grains with low GOS values are also visible.

To further analyze the microstructural evolution during hot rolling in characteristic bands, EBSD analysis was performed at higher magnification. Figure 15 presents the EBSD maps for the band containing fine α phase grains. Grain boundaries were overlaid on the maps based on the misorientation angle (θ). LAGBs, with a misorientation angle θ less than 15°, are marked in white, while HAGBs, with a misorientation angle θ greater than 15°, are marked in black. LAGBs are approximately evenly distributed with slightly higher density in regions where finer or needle-like α phase grains are present. This indicates the occurrence of α phase globularization in this area. GOS values concerning the β phase indicate that the matrix is almost entirely recrystallized, and DRV grains are visible.

Figure 16 presents the results of EBSD analysis for the band of β phase grains. LAGBs are visible and accumulated within the primary β grain boundaries. Different grain orientations are observed within the β grains, indicating the formation of a substructure during deformation. These features suggest that the dominant microstructural evolution mechanism in this band is DRV. This is further confirmed by the GOS map, where the β grains have a medium GOS value. However, DRV also occurs in this band. Recrystallized β grains are particularly visible near the intersection of primary grain boundaries, where the accumulation of energy from

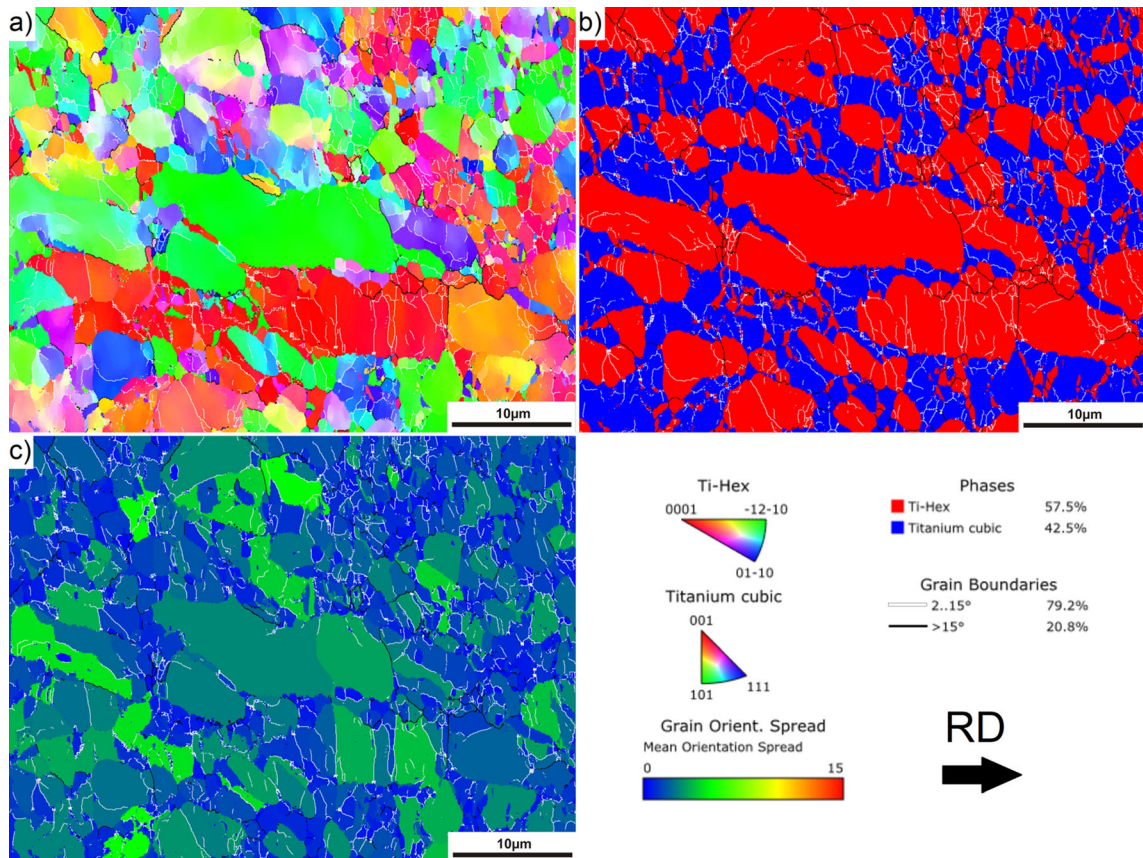


Fig. 15—EBSD maps of band of fine α grains of hot-rolled Ti-5553 compact; (a) IPF map; (b) phase map; (c) GOS map. Black lines and white lines indicate HAGBs and LAGBs, respectively.

dislocations is highest and acts as a driving force for nucleation of new grains.

EDS analysis was conducted to investigate the chemical composition differences between the regions rich in α -phase grains and those primarily composed of β -phase in the microstructure obtained after the rolling process. The results of the analysis are presented in Figure 17. It is evident that the regions containing spherical α -phase particles exhibit higher concentrations of Ti and Al, while the proportions of Mo and Cr are significantly reduced compared to the regions consisting of the β phase.

The method of manufacturing titanium alloys has a significant impact on their microstructure, relative density, and, consequently, on their strength properties. When elemental powders are used as starting materials, there is a possibility of local inhomogeneities in the chemical composition, which can have consequences in terms of local inhomogeneities in chemical composition.^[45] Therefore, it was assumed that as a result of the hot deformation applied, in addition to compaction, obtaining the desired microstructure, and homogenization of the distribution of the alloying elements should happen, leading to improved homogeneity in the material's properties. To verify this assumption, the distribution map of the alloying elements after hot deformation was analyzed in terms of solubility and

the diffusion process of the elements into the different phases.

The distribution of alloying elements depends on their solubility, the diffusion rate in a given phase, and the duration of diffusion. During heating and annealing, the mobility of atoms increases, facilitating diffusion processes. In titanium alloys, the alloying elements are distributed between the phases. The α -phase tends to have higher concentrations of titanium and aluminum, while Mo accumulates at the interface due to its slower diffusivity compared to other alloying elements.^[46] The distribution of alloying elements stabilizing the β -phase was observed to be uniform in the β -phase. Significant differences were observed for the α phase, where there was a higher concentration of aluminum and titanium and a lower concentration of β -phase-stabilizing elements, particularly Mo and Cr. The distribution of alloying elements depends on several factors. The first is their diffusivity in each phase. Aluminum has 20 times higher diffusivity in the α phase than in the β phase, while the trend is the opposite for the β phase-stabilizing elements.^[47] It is also important to note that the presence of one alloying element can reduce the diffusivity of another. For example, the addition of approximately 5 pct Al reduces the diffusivity of Cr from 2.839×10^{-16} to 1.183×10^{-16} m²/s.^[48]

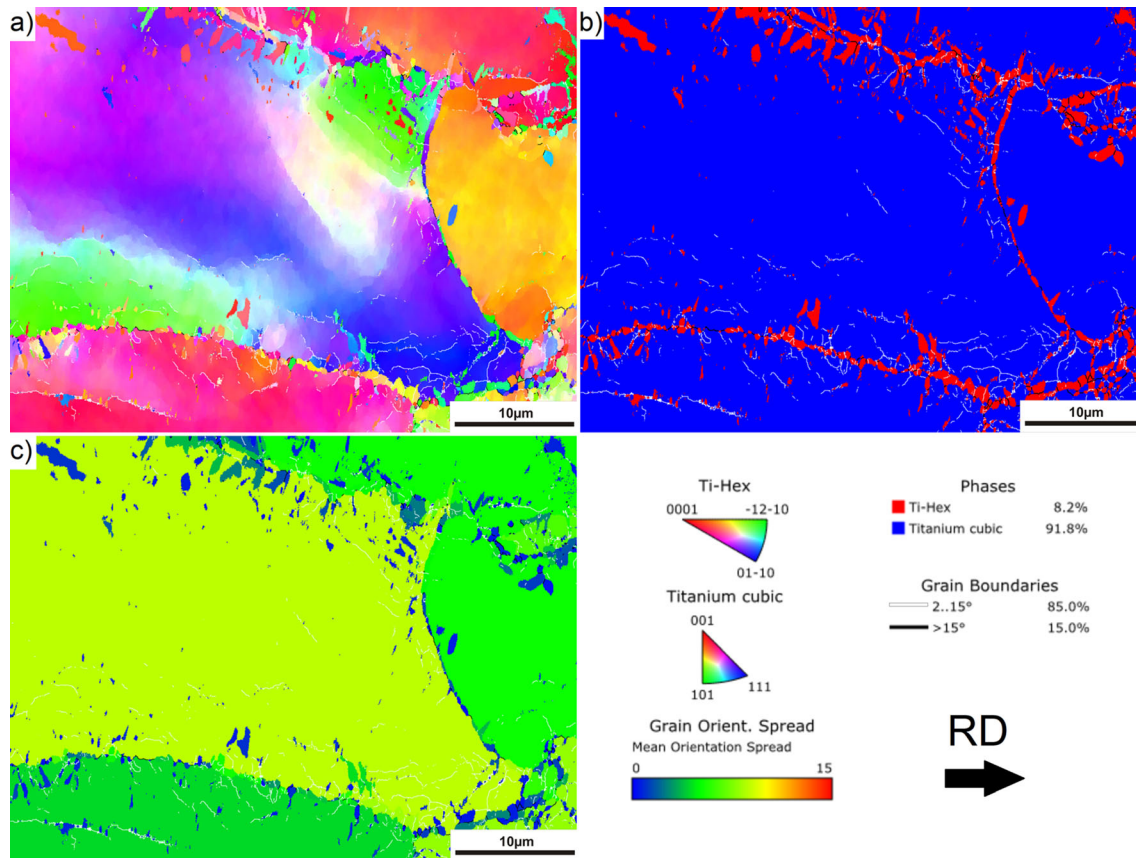


Fig. 16—EBSD maps of band of β grains of hot-rolled Ti-5553 compact; (a) IPF map; (b) phase map; (c) GOS map. Black lines and white lines indicate HAGBs and LAGBs, respectively.

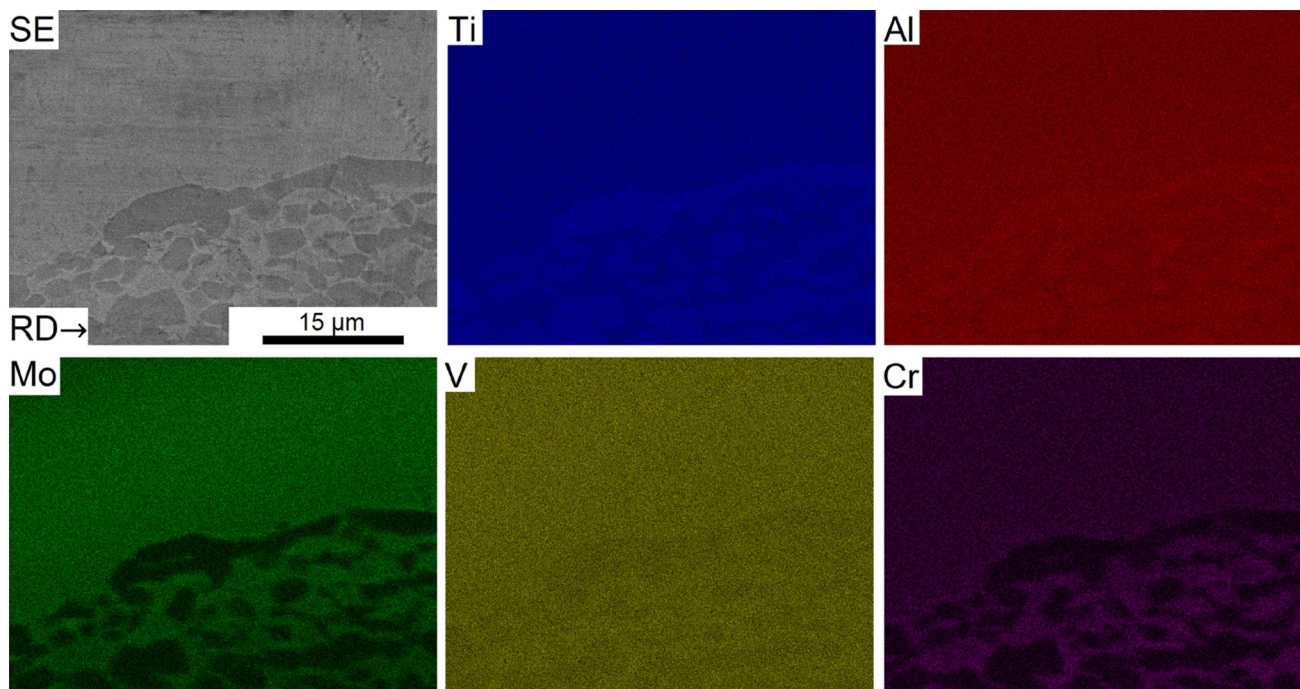


Fig. 17—Element distribution maps for hot-rolled Ti-5553 alloy compact.

Another factor is the duration of exposure to high temperatures. As discussed earlier, an increase in temperature promotes diffusion processes, allowing the system to approach an equilibrium state of elemental concentration. If the high-temperature exposure is too short, complete diffusion of the alloying element from one phase to a neighboring phase may not occur.^[45] This is particularly evident when the diffusion efficiency of a given element in a phase is relatively low (for example, Cr in the α phase).

The deformation process started above the β -transus temperature leading to the dissolution of a significant portion of the α grains and the even distribution of alloying elements within the β phase matrix. As the

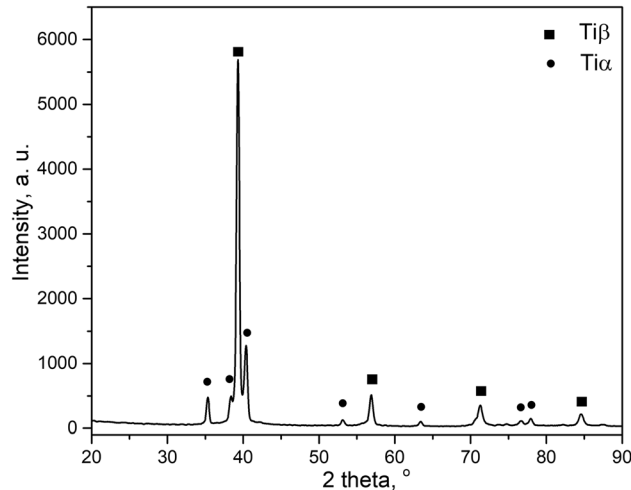


Fig. 18—XRD pattern of hot-rolled Ti-5553 compact.

hot-rolling process proceeded, the temperature dropped below the phase transformation temperature, which the case of titanium alloys is a diffusion-controlled transformation, so there was a redistribution of the alloying elements. In terms of the α phase, the duration of the process was sufficient for the components stabilizing the β phase to diffuse into the matrix. In contrast, the secondary α phase visible in the EBSD maps (Figure 16), which is precipitated during cooling from the β phase in the form of fine needles, contains a relatively higher concentration of elements such as Mo, V, or Cr. Consequently, it is not as clearly visible in the element distribution maps as the primary α grains.

Figure 18 presents the XRD pattern of the hot-rolled Ti-5553 compact. Similar to the as-pressed compact, the analysis confirmed the presence of a hexagonal α phase and a β phase with a BCC structure. However, due to the deformation process that occurred above the β -transus temperature, the microstructure was remodeled and the contribution of the two phases changed. A comparison of the XRD patterns in Figures 2(c) and 18 reveals that the peaks corresponding to the α phase are less prominent in the hot-rolled alloy compared to those observed in the compact.

Figure 19(a) displays the engineering stress–engineering strain curves of the as-pressed and hot-rolled Ti-5553 compact. The tensile strength of the Ti-5553 alloy compact was relatively low at 757 ± 19 MPa, with an elongation of 2 ± 0.1 pct. Obtained tensile strength can be compared to the results shown by Sen *et al.*^[49] for a Ti-5553 alloy made by a conventional method and annealed above the β -transus temperature, with a microstructure composed only of β grains (770 MPa), but the elongation is significantly lower (22 pct). The

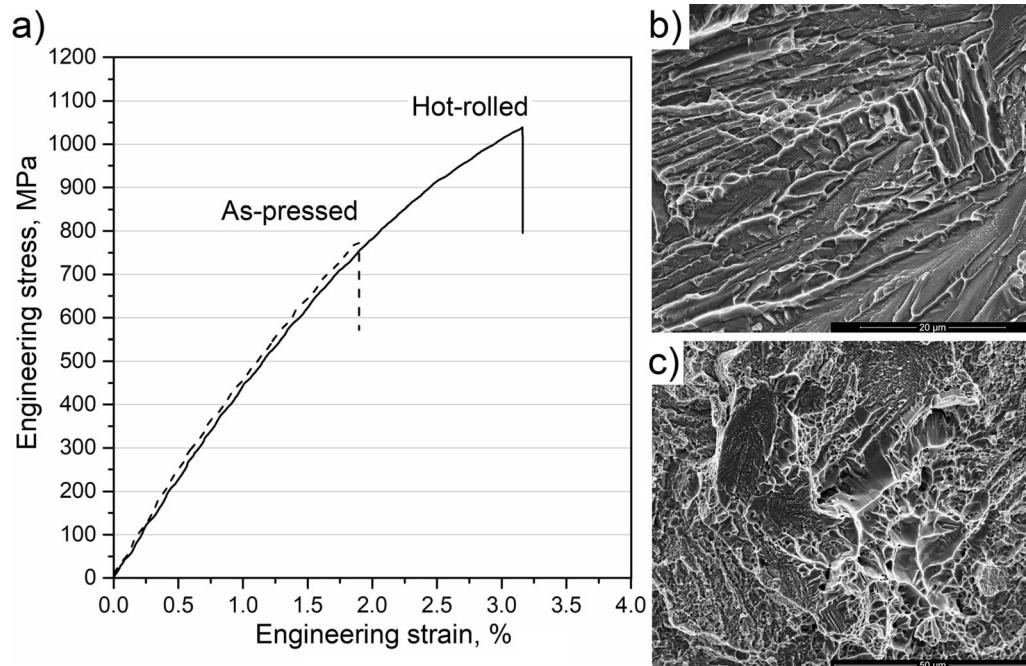


Fig. 19—(a) Engineering stress–engineering strain curves of as-pressed and hot-rolled Ti-5553 compact, SEM micrographs of the fracture surface of (b) as-pressed and (c) hot-rolled Ti-5553 compact.

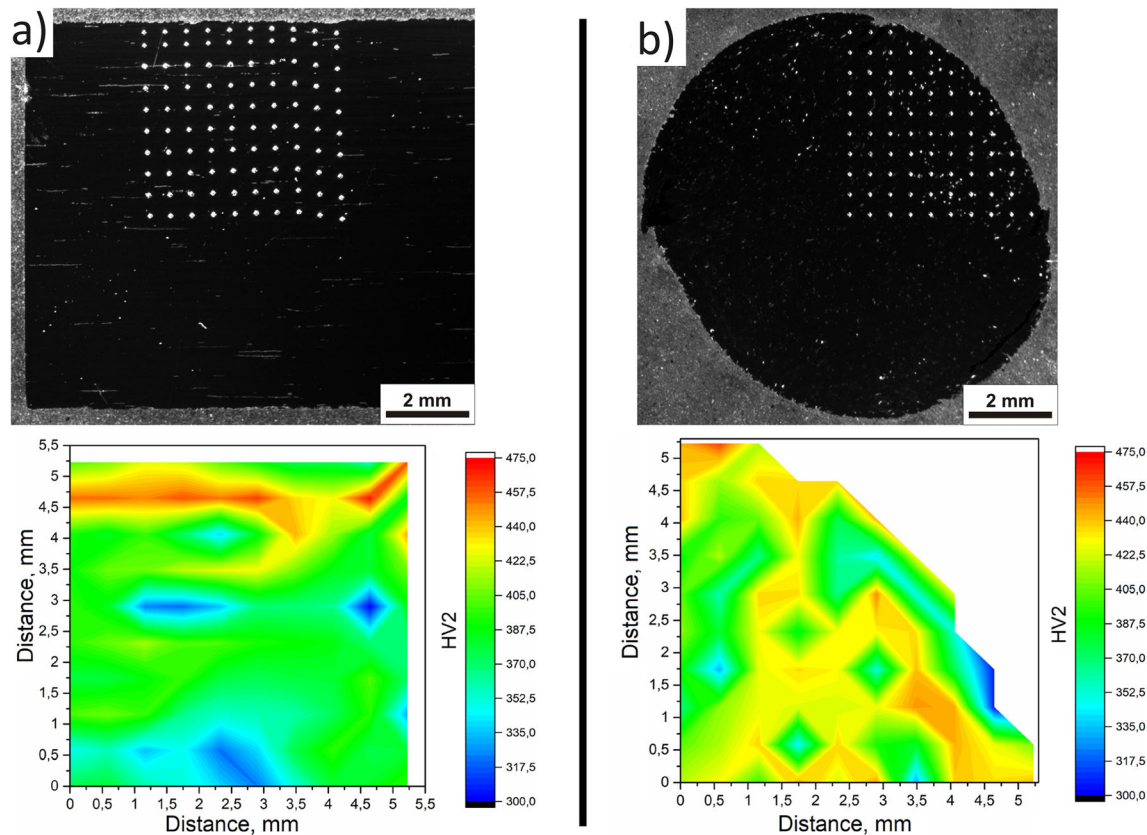


Fig. 20—Macrophotographs of individual sections of a hot-rolled Ti-5553 alloy compact with visible indentation after HV2 measurements and the corresponding hardness maps: (a) longitudinal section, (b) cross section.

low ductility and lack of a clear yield stress suggested the brittle nature of the fracture, as confirmed by SEM microphotographs of the fracture surface shown in Figure 19(b). The transgranular fracture surfaces are observed to run along the colony of α -phase plates. After hot rolling, the tensile strength of the compact increased by approximately 250 MPa reaching 1009 ± 26 MPa. The elongation also increased and was 3.2 ± 0.03 pct. Similar tensile strength was observed for the Ti-5553 alloy obtained by casting with large aspect ratio of α precipitates^[49] and also for the same alloy hot rolled in the two-phase range, without heat treatment.^[50] Nevertheless, in both cases, the authors of the study showed significantly higher ductility of the alloy (16 and 29.1 pct, respectively). The increased ductility compared to the material in the hot-pressed state is also evident from the observation of the fracture surface shown in Figure 19(c). A higher proportion of dimples is observed in relation to intergranular fracture surfaces, indicating the ductile nature of the fracture as a result of the microstructure remodeling after hot rolling.

The average hardness after hot rolling was 409 ± 37 HV2 compared to the starting material, (401 ± 22 HV2), the hardness of the rod increased only slightly. Figure 20 displays the hardness distribution maps, which reveal the effect of strain on the material's hardness as well as the variation across the cross section

where the measurements were taken. The macrophotographs illustrate the measurement methodology employed. In the longitudinal section at the center of the rod, the hardness is relatively uniform, ranging between 375 and 400 HV2. However, a noticeable increase in hardness is observed in the region near the edge, where values reach up to 450 HV2. On the cross section, generally higher hardness is recorded, ranging between 425 and 440 HV2. The FEM numerical analysis of the hot-rolling process provided insight into the strain intensity distribution, indicating that the material experiences more deformation in the area near the contact surface with the rollers. This suggests that surface hardening may occur, potentially leading to localized improvements in toughness properties. The obtained HV2 hardness distribution maps support the results obtained from the FEM modeling, confirming the accuracy of the simulation.

IV. CONCLUSIONS

The hot deformation behavior of the metastable titanium alloy obtained by the BEPM approach was studied. Based on the flow curves, constitutive model, processing maps, FEM analysis, and microstructure observations of the material after deformation, the following conclusions have been elaborated:

- (1) The behavior of the Ti-5553 alloy compact under hot deformation conditions was obtained from hot compression tests at different combinations of thermomechanical parameters. The collected data allowed to development of a comprehensive characterization of the phenomena accompanying the hot deformation of the alloy.
- (2) The constitutive model, deformation activation energy map, and processing maps were developed based on flow curves. The processing window has been defined for strain rates from 0.1 to 2.0 s⁻¹ and temperatures in the range from 900 °C to 1000 °C.
- (3) The microstructure analysis confirmed the results of the DMM analysis. It was observed that flow localization was present at the combination of parameters indicated as unfavorable during hot deformation. For the processing window parameters, a homogeneous and recrystallized microstructure was found.
- (4) Based on the FEM simulations results, it was confirmed that the Ti-5553 compact could be successfully hot rolled under the proposed conditions without failure. FEM analysis made it possible to determine favorable hot-rolling parameters within the ranges of the developed processing window.
- (5) Verification of the developed thermomechanical deformation parameters was carried out based on the hot-rolling tests. Evaluation of the quality of the obtained material showed that the applied parameters led to products fully compacted, with controlled microstructure and significant increase in tensile strength from 757 to 1009 MPa.

ACKNOWLEDGMENTS

The financial support of the Polish Ministry of Science and Higher Education is gratefully acknowledged (AGH-UST Statutory Research Project No. 16.16.110.663). Research project is partly supported by program, “Excellence Initiative – Research University” for the AGH University of Krakow.

CONFLICT OF INTEREST

On behalf of all authors, the corresponding author states that there is no conflict of interest.

REFERENCES

1. J.D. Cotton, R.D. Briggs, R.R. Boyer, S. Tamirisakandala, P. Russo, N. Shchetnikov, and J.C. Fanning: *JOM*, 2015, vol. 67, pp. 1281–1303.
2. J.C. Williams and R.R. Boyer: *Metals*, 2020, <https://doi.org/10.3390/met10060705>.
3. J. Capus: *Met. Powder Rep.*, 2017, vol. 72, pp. 384–88.
4. E. Calvert, B. Wynne, N. Weston, A. Tudball, and M. Jackson: *J. Mater. Process. Technol.*, 2018, vol. 254, pp. 158–70.

5. E.V. Pereloma, D.G. Savvakina, A. Carman, A.A. Gazder, and O.M. Ivasishin: *Key Eng. Mater.*, 2012, vol. 520, pp. 49–56.
6. L. Bolzoni, E.M. Ruiz-Navas, and E. Gordo: *Mater. Sci. Eng. C*, 2015, vol. 49, pp. 400–07.
7. M. Ahmed, D.G. Savvakina, O.M. Ivasishin, and E.V. Pereloma: *J. Alloys Compd.*, 2017, vol. 714, pp. 610–18.
8. C.-M. Li, L. Huang, C.-L. Li, S.-X. Hui, Y. Yu, M.-J. Zhao, S.-Q. Guo, and J.-J. Li: *Rare Met.*, 2022, <https://doi.org/10.1007/s12598-021-01861-7>.
9. Q. Zhao, Y. Chen, Y. Xu, R. Torrens, L. Bolzoni, and F. Yang: *Mater. Des.*, 2021, vol. 200, 109457.
10. J. Fan, H. Kou, Y. Zhang, L. Germain, K. Hua, L. Tang, C. Esling, and J. Li: *J. Alloys Compd.*, 2019, vol. 770, pp. 183–93.
11. Y.C. Lin, J. Huang, H.B. Li, and D.D. Chen: *Vacuum*, 2018, vol. 157, pp. 83–91.
12. O. Lypchanskyi, T. Śleboda, A. Łukaszek-Solek, K. Zygula, and M. Wojtaszek: *Materials*, 2021, vol. 14, p. 2021.
13. K. Zygula, M. Wojtaszek, O. Lypchanskyi, T. Śleboda, G. Korpała, and U. Prah: *Metall. Mater. Trans. A*, 2019, vol. 50A, pp. 5314–23. <https://doi.org/10.1007/s11661-019-05434-3>.
14. K. Zygula, M. Wojtaszek, T. Śleboda, O. Lypchanskyi, M. Rumiński, G. Korpała, and U. Prah: *Procedia Manuf.*, 2020, vol. 50, pp. 546–51.
15. O. Lypchanskyi, T. Śleboda, K. Zygula, A. Łukaszek-Solek, and M. Wojtaszek: *Materials*, 2020, vol. 13, p. 3629.
16. L. Kang and C. Yang: *Adv. Eng. Mater.*, 2019, vol. 21, p. 1801359.
17. K. Zygula and M. Wojtaszek: *Arch. Metall. Mater.*, 2020, vol. 65, pp. 287–93.
18. K. Zygula, M. Wojtaszek, T. Śleboda, S. Lech, O. Lypchanskyi, G. Korpała, and U. Prah: *Metall. Mater. Trans. A*, 2021, vol. 52A, pp. 1699–1713.
19. D. Gomez-Marquez, E. Ledesma-Orozco, R. Hino, E. Aguilera-Gomez, G. Korpała, and U. Prah: *SN Appl. Sci.*, 2022, <https://doi.org/10.1007/s42452-022-05093-x>.
20. P. Christiansen, P.A.F. Martins, and N. Bay: *Exp. Mech.*, 2016, vol. 56, pp. 1271–79.
21. Q. Zhao, F. Yang, R. Torrens, and L. Bolzoni: *Int. J. Refract. Met. Hard Mater.*, 2020, vol. 90, 105235.
22. J. Sun, Z. Zhang, M. Zhang, F. Jiang, and M. Ding: *J. Alloys Compd.*, 2016, vol. 663, pp. 769–74.
23. Y.D. Im, Y.K. Lee, and K.H. Song: *Mater. Sci. Eng. A*, 2018, vol. 725, pp. 479–87.
24. C. Li, L. Huang, M. Zhao, S. Guo, and J. Li: *Mater. Sci. Eng. A*, 2021, vol. 814, 141231.
25. Q. Zhao, F. Yang, R. Torrens, and L. Bolzoni: *Mater. Des.*, 2019, vol. 169, 107682.
26. H. Matsumoto, M. Kitamura, Y. Li, Y. Koizumi, and A. Chiba: *Mater. Sci. Eng. A*, 2014, vol. 611, pp. 337–44.
27. M.L. Wasz, F.R. Brotzen, R.B. McLellan, and A.J. Griffin: *Int. Mater. Rev.*, 1996, vol. 41, pp. 1–12.
28. X. Xu, Y. Han, C. Li, P. Nash, D. Mangabhai, and W. Lu: *J. Mater. Res.*, 2015, vol. 30, pp. 1056–64.
29. Y.V.R.K. Prasad and T. Seshacharyulu: *Mater. Sci. Eng. A*, 1998, vol. 243, pp. 82–88.
30. B. Liu, Y. Liu, W. Zhang, and J.S. Huang: *Intermetallics*, 2011, vol. 19, pp. 154–59.
31. J. Zhang, H. Di, H. Wang, K. Mao, T. Ma, and Y. Cao: *J. Mater. Sci.*, 2012, vol. 47, pp. 4000–11.
32. W. Chuan and H. Liang: *Vacuum*, 2018, vol. 156, pp. 384–401.
33. F. Warchomicka, C. Poletti, and M. Stockinger: *Mater. Sci. Eng. A*, 2011, vol. 528, pp. 8277–85.
34. Y.V.R.K. Prasad, H.L. Giegel, S.M. Doraivelu, J.C. Malas, J.T. Morgan, K.A. Lark, and D.R. Barker: *Metall. Trans. A*, 1984, vol. 15, pp. 1883–92.
35. S. Nemat-Nasser, W.G. Guo, and J.Y. Cheng: *Acta Mater.*, 1999, vol. 47, pp. 3705–20.
36. S.L. Semiatin, V. Seetharaman, and I. Weiss: *Mater. Sci. Eng. A*, 1999, vol. 263, pp. 257–71.
37. A. Dehghan-Manshadi and R.J. Dippenaar: *Mater. Sci. Eng. A*, 2012, vol. 552, pp. 451–56.
38. S. Mandal, B.T. Gockel, S. Balachandran, D. Banerjee, and A.D. Rollett: *Int. J. Plast.*, 2017, vol. 94, pp. 57–73.
39. Y. Sun, B. Huang, D.A. Puleo, and I.S. Jawahir: *Procedia CIRP*, 2015, vol. 31, pp. 477–82.

40. Y. Kaynak, A. Gharibi, and M. Ozkutuk: *Int. J. Adv. Manuf. Technol.*, 2018, vol. 94, pp. 1411–28.
41. M. Wojtaszek, G. Korpała, T. Śleboda, K. Zygula, and U. Prahł: *Metall. Mater. Trans. A*, 2020, vol. 51A, pp. 5790–5805.
42. S.I. Wright, M.M. Nowell, and D.P. Field: *Microsc. Microanal.*, 2011, vol. 17, pp. 316–29.
43. J. Lei, W. Zhu, L. Chen, Q. Sun, L. Xiao, and J. Sun: *Mater. Today Commun.*, 2020, vol. 23, 100873.
44. Q.Y. Zhao, F. Yang, R. Torrens, and L. Bolzoni: *Mater. Charact.*, 2019, vol. 149, pp. 226–38.
45. A. Carman, L.C. Zhang, O.M. Ivasishin, D.G. Savvakina, M.V. Matviychuk, and E.V. Pereloma: *Mater. Sci. Eng. A*, 2011, vol. 528, pp. 1686–93.
46. S. Nag, R. Banerjee, J.Y. Hwang, M. Harper, and H.L. Fraser: *Philos. Mag.*, 2009, vol. 89, pp. 535–52.
47. H. Nakajima and M. Koiwa: *ISIJ Int.*, 1991, vol. 31, pp. 757–66.
48. M. Ahmed, A.A. Gazder, D.G. Savvakina, O.M. Ivasishin, and E.V. Pereloma: *J. Mater. Sci.*, 2012, vol. 47, pp. 7013–25.
49. M. Sen, S. Suman, T. Banerjee, A. Bhattacharjee, and S.K. Kar: *Mater. Sci. Eng. A*, 2019, vol. 753, pp. 156–67.
50. Z.X. Du, S.L. Xiao, Y.P. Shen, J.S. Liu, J. Liu, L.J. Xu, F.T. Kong, and Y.Y. Chen: *Mater. Sci. Eng. A*, 2015, vol. 631, pp. 67–74.

Publisher's Note Springer Nature remains neutral with regard to jurisdictional claims in published maps and institutional affiliations.

Springer Nature or its licensor (e.g. a society or other partner) holds exclusive rights to this article under a publishing agreement with the author(s) or other rightsholder(s); author self-archiving of the accepted manuscript version of this article is solely governed by the terms of such publishing agreement and applicable law.